

























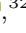




## First results from the PanRadio GRB Collaboration: the 400-day afterglow of GRB 230815A

JAMES K. LEUNG <sup>1, 2, 3</sup> GEMMA E. ANDERSON <sup>4</sup> ALEXANDER J. VAN DER HORST <sup>5</sup> CLAIRE MORLEY <sup>4</sup>  
BENJAMIN SCHNEIDER <sup>6, 7</sup> FABIO DE COLLE <sup>8</sup> OM SHARAN SALAFIA <sup>9, 10</sup> GIANCARLO GHIRLANDA <sup>9, 10</sup>  
SARAH L. CHASTAIN <sup>11, 12</sup> ADELLE J. GOODWIN <sup>4</sup> ASHNA GULATI <sup>13, 14, 15</sup> LAUREN RHODES <sup>16, 17</sup>  
STUART D. RYDER <sup>18, 19</sup> ASHLEY A. CHRIMES <sup>20, 21</sup> VALERIO D'ELIA <sup>22</sup> MATHIEU DE BONY DE LAVERGNE <sup>23, 24</sup>  
MASSIMILIANO DE PASQUALE <sup>25</sup> ANTONIO DE UGARTE POSTIGO <sup>6</sup> DIETER H. HARTMANN <sup>26</sup>  
BENJAMIN P. GOMPERTZ <sup>27, 28</sup> ANDREW J. LEVAN <sup>21, 29</sup> TARA MURPHY <sup>13, 15</sup> GAVIN P. ROWELL <sup>30</sup>  
THOMAS D. RUSSELL <sup>31</sup> FABIAN SCHÜSSLER <sup>24</sup> RHAANA L. C. STARLING <sup>32</sup> NIAL R. TANVIR <sup>32</sup>  
SUSANNA D. VERGANI <sup>33</sup> AND RALPH A.M.J. WIJERS <sup>34</sup>

- <sup>1</sup>David A. Dunlap Department of Astronomy and Astrophysics, University of Toronto, 50 St. George Street, Toronto, ON M5S 3H4, Canada
- <sup>2</sup>Dunlap Institute for Astronomy and Astrophysics, University of Toronto, 50 St. George Street, Toronto, ON M5S 3H4, Canada
- <sup>3</sup>Racah Institute of Physics, The Hebrew University of Jerusalem, Jerusalem 91904, Israel
- <sup>4</sup>International Centre for Radio Astronomy Research, Curtin University, GPO Box U1987, Perth, WA 6845, Australia
- <sup>5</sup>Department of Physics, George Washington University, 725 21st St NW, Washington, DC 20052, USA
- <sup>6</sup>Aix Marseille University, CNRS, CNES, LAM, Marseille, France
- <sup>7</sup>Massachusetts Institute of Technology, Kavli Institute for Astrophysics and Space Research, Cambridge, Massachusetts, USA
- <sup>8</sup>Instituto de Ciencias Nucleares, Universidad Nacional Autónoma de México, A. P. 70-543 04510 D. F. Mexico
- <sup>9</sup>INAF - Osservatorio Astronomico di Brera, via E. Bianchi 46, I-23807 Merate (LC), Italy
- <sup>10</sup>INFN - Sezione di Milano-Bicocca, Piazza della Scienza 3, 20126 Milano (MI), Italy
- <sup>11</sup>Department of Physics and Astronomy, University of New Mexico, Albuquerque, NM 87131, USA
- <sup>12</sup>Department of Physics & Astronomy, Texas Tech University, Box 41051, Lubbock, TX, 79409-1051, USA
- <sup>13</sup>Sydney Institute for Astronomy, School of Physics, The University of Sydney, NSW 2006, Australia
- <sup>14</sup>CSIRO Space and Astronomy, PO Box 76, Epping, NSW 1710, Australia
- <sup>15</sup>ARC Centre of Excellence for Gravitational Wave Discovery (OzGrav), Hawthorn, VIC 3122, Australia
- <sup>16</sup>Trottier Space Institute at McGill, 3550 Rue University, Montreal, Quebec H3A 2A7, Canada
- <sup>17</sup>Department of Physics, McGill University, 3600 Rue University, Montreal, Quebec H3A 2T8, Canada
- <sup>18</sup>School of Mathematical and Physical Sciences, Macquarie University, NSW 2109, Australia
- <sup>19</sup>Astrophysics and Space Technologies Research Centre, Macquarie University, Sydney, NSW 2109, Australia
- <sup>20</sup>European Space Agency (ESA), European Space Research and Technology Centre (ESTEC), Keplerlaan 1, 2201 AZ Noordwijk, The Netherlands
- <sup>21</sup>Department of Astrophysics/IMAPP, Radboud University Nijmegen, P.O. Box 9010, Nijmegen, 6500 GL, The Netherlands
- <sup>22</sup>Space Science Data Center (SSDC) - Agenzia Spaziale Italiana (ASI), Via del Politecnico snc, 00133 Roma, Italy
- <sup>23</sup>Aix Marseille Université, CNRS/IN2P3, CPPM, Marseille, France
- <sup>24</sup>IRFU, CEA, Université Paris-Saclay, F-91191 Gif-sur-Yvette, France
- <sup>25</sup>University of Messina, MIFT Department, via F. S. D'Alcontres 31, Messina, 98166, Italy
- <sup>26</sup>Department of Physics and Astronomy, Clemson University, Clemson, SC 29634-0978, USA
- <sup>27</sup>School of Physics and Astronomy, University of Birmingham, Birmingham B15 2TT, UK
- <sup>28</sup>Institute for Gravitational Wave Astronomy, University of Birmingham, Birmingham B15 2TT
- <sup>29</sup>Department of Physics, University of Warwick, Coventry, CV4 7AL, UK
- <sup>30</sup>School of Physics, Chemistry and Earth Sciences, The University of Adelaide, Adelaide SA 5005, Australia
- <sup>31</sup>INAF, Istituto di Astrofisica Spaziale e Fisica Cosmica, Via U. La Malfa 153, I-90146 Palermo, Italy
- <sup>32</sup>School of Physics and Astronomy, University of Leicester, University Road, Leicester LE1 7RH, UK
- <sup>33</sup>LUX, Observatoire de Paris, PSL University, CNRS, Sorbonne University, 92190 Meudon, France
- <sup>34</sup>Anton Pannekoek Institute for Astronomy, University of Amsterdam, Science Park 904, P.O. Box 94249, 1090 GE Amsterdam, The Netherlands

(Received xxx x, 202x; Revised xxx x, 202x; Accepted xxx x, 202x)

## ABSTRACT

We introduce the PanRadio Gamma-ray Burst (GRB) program carried out on the Australia Telescope Compact Array: a systematic, multi-year, radio survey of all southern *Swift* GRB events, comprehensively following the multi-frequency evolution of their afterglows from within an hour to years post-burst. We present the results of the 400-day observing campaign following the afterglow of long-duration (collapsar) GRB 230815A, the first one detected through this program. Typically, GRB 230815A would not otherwise receive traditional radio follow-up, given it has no known redshift and lacks comprehensive multi-wavelength follow-up due to its high line-of-sight extinction with  $A_V = 2.3$ . We found its early X-ray jet break at  $\sim 0.1$  days post-burst to be at odds with the evolution of the multi-frequency radio light curves that were traced over an unusually long duration of 400 days. The radio light curves approximately evolved (with minor deviations) according to the standard self-similar expansion for a relativistic blast wave in a homogeneous environment prior to jet break, showing no evidence for evolution in the microphysical parameters describing the electron acceleration processes. We reconcile these features by proposing a two-component jet: the early X-ray break originates from a narrow component with a half-opening angle  $\sim 2.1^\circ$ , while the evolution of the radio afterglow stems from a wider component with a half-opening angle  $\gtrsim 35^\circ$ . The PanRadio GRB program will establish a sample of comprehensively followed GRBs, where a rigorous inspection of their microphysical and dynamical parameters can be performed, thereby revealing the diversity of features in their outflows and environments.

*Keywords:* Gamma-ray bursts(629) — Time domain astronomy(2109)

## 1. INTRODUCTION

Ultra-relativistic collimated outflows are thought to produce gamma-ray bursts (GRBs), which for a brief moment, radiate enough energy to outshine the rest of the Universe. These outflows are launched by a newborn, rapidly-spinning compact object following the collapse of a massive star or the merger of a compact binary (Paczynski 1986; Rees & Meszaros 1992; Woosley 1993; Mészáros & Rees 1997). As the outflow expands ballistically within the circumburst medium (CBM) that surrounds the progenitor, it gives rise to a “forward” shock, propagating outwards into the CBM. When the shock sweeps up a sufficient amount of mass, the ejecta significantly decelerate and drive a “reverse” shock, propagating towards the inner layers of the outflow in the comoving frame of the blast wave. Diffusive acceleration of electrons within these shocks leads to synchrotron and inverse Compton emission, producing a GRB “afterglow” detectable from radio to very-high-energy (TeV) gamma-rays (e.g., Costa et al. 1997; Frail et al. 1997; van Paradijs et al. 1997; Abdalla et al. 2019; MAGIC Collaboration et al. 2019).

As sites of particle acceleration, the forward and reverse shocks produce two distinct synchrotron components detectable at radio (gigahertz) frequencies, hence a forward-reverse shock model is needed for interpreting the early afterglow. The broadband spectrum of each synchrotron component is described by the peak flux density and the characteristic break frequencies,

which all evolve as a function of time (Sari et al. 1998; Panaitescu & Kumar 2000; Granot & Sari 2002; Gao et al. 2013). The observed spectral evolution can then be related to the physical properties describing the system, such as the energetics of the outflow, the density and structure of the CBM (by extension, the mass-loss history of the progenitor in the case of GRBs originating from collapsars), and the shock microphysics (i.e., the fraction of energy in the magnetic fields and emitting electron population, as well as the Lorentz factor distribution). While the forward shock emission can take tens to hundreds of days to peak at gigahertz frequencies (Chandra & Frail 2012), the reverse shock often peaks and fades away within a day to a few days post-burst (e.g., Anderson et al. 2014, 2018). This highlights the need for high-cadence, multi-frequency radio observations from early (less than a day post-burst) through to late times (more than a year post-burst) to properly constrain and disentangle the properties of the reverse and forward shock components.

Comprehensive radio monitoring of an afterglow will therefore enable a complete and rigorous inspection of the dynamical and shock parameters that describe the blast wave and its environment. Despite GRBs being the most powerful explosions in the Universe, we still lack a complete picture of the generation and properties of the outflows and how they impact their surrounding environment. This is in large part due to limited radio observations of GRBs as they are difficult to be

rapidly scheduled following the appearance of a new event, which in turn is difficult to be followed up until late times (more than a year post-burst) due to the limited number of radio interferometer arrays in the world with sufficient sensitivity for this task; for a brief review of radio afterglow observations in the first 14 years since the discovery of the afterglow (1997 to 2011), see [Chandra & Frail \(2012\)](#).

The GRBs that have radio follow-up in the literature have often been selectively-targeted based on known properties — such as the existence of an optical and/or X-ray counterpart, a low redshift, a high gamma-ray fluence (e.g., in the case of GRB 221009A; [Bright et al. 2023](#); [Laskar et al. 2023](#); [Rhodes et al. 2024](#)), those suspected to be optically “dark” bursts (e.g., [Djorgovski et al. 2001](#); [Jakobsson et al. 2004](#); [van der Horst et al. 2009](#)), candidate lensing events (e.g., [Giarratana et al. 2023](#); [Leung et al. 2025](#)), or those suspected to be at high redshift (e.g., [Salvaterra 2015](#); [Fausey et al. 2025](#), and references therein) — which leads to inherent biases in our understanding of their phenomenological and physical properties. Of those that have radio follow-up, an even smaller subset are followed to very late times. Indeed, in the three decades since the discovery of the first afterglow, only approximately 10 GRBs had comprehensive multi-wavelength coverage extending to more than a year post-burst (e.g., GRBs 970508, 980703, 000418, 030329, 130427A, 170817A, 171205A, 190829A, 221009A; [Frail et al. 2000, 2003](#); [Berger et al. 2001](#); [van der Horst et al. 2008, 2014](#); [Makhathini et al. 2021](#); [Leung et al. 2021](#); [Maity & Chandra 2021](#); [Rhodes et al. 2020](#); [Salafia et al. 2022](#); [Laskar et al. 2023](#); [Rhodes et al. 2024](#)).

As a result, the transition of the blast wave to the non-relativistic regime and the deep-Newtonian regime, often occurring years post-burst, is not very well constrained for most GRBs. In the non-relativistic regime, the blast wave has decelerated to sub-relativistic Lorentz factors and becomes quasi-spherical, where the dynamics can be approximately described by the Sedov-von Neumann-Taylor self-similar solution (e.g., [Livio & Waxman 2000](#); [Frail et al. 2000](#); [Zhang & MacFadyen 2009](#); [De Colle et al. 2012](#); [van Eerten & MacFadyen 2012](#)). At even later times, when the bulk of the shocked electrons become non-relativistic, the blast wave enters the deep-Newtonian regime, resulting in a shallower decay than that predicted in the non-relativistic regime ([Sironi & Giannios 2013](#)). Radio monitoring of the GRB after the blast wave has entered the non-relativistic and deep-Newtonian phase is important because it allows for accurate calorimetry regardless of the initial jet structure ([Frail et al. 2000](#)). Calorimetric calculations have only

been performed in a few works and for a small sample of bursts (e.g., [Frail et al. 2000, 2005](#); [van der Horst et al. 2008](#); [Shivvers & Berger 2011](#)) so a precise distribution of GRB energy budgets is still lacking. Additionally, the tracing of the radio spectral evolution into late times allows for the density profile of the CBM to be mapped to a larger radius (and further back in time pre-explosion), revealing information about both the host galaxy environment and mass-loss history of the progenitor. For instance, changes in the density profile are expected at the wind termination-shock radius (e.g., [Pe’er & Wijers 2006](#); [Gendre et al. 2007](#); [Schulze et al. 2011](#)), the interface between the progenitor stellar winds and the surrounding interstellar medium (ISM). The transition could explain why some long GRBs are better explained by an ISM environment (a dense ISM may suppress the propagation of the stellar wind; see e.g., [Chrimes et al. 2022](#), and references therein); however, no observations to date have convincingly shown this transition. A recent probe of the CBM environment at very late times for GRB 171205A found that even at over 1 000 days post-burst, the afterglow was consistent with the burst exploding into a stellar-wind environment with no signs of any regime transition ([Leung et al. 2021](#); [Maity & Chandra 2021](#)). Following events to these very late times at higher energies (than radio) is difficult but not unprecedented; e.g., the X-ray afterglow of GRB 130427A was followed for  $\sim 80$  Ms (or  $\sim 1\,000$  days) and similarly showed an unperturbed decay across three orders of magnitude in time ([De Pasquale et al. 2016](#)).

These results (or lack thereof) motivated the Panoptic Radio View of Gamma-ray Bursts (“PanRadio GRB”) program, a comprehensive radio follow-up program of GRBs. The PanRadio GRB program will provide a more complete, more unbiased, multi-frequency (1 – 50 GHz) and high cadence radio view of GRBs from early ( $< 1$  day post-burst) through to late ( $> 1$  year post-burst) times. The aim of the program is to ultimately determine the true prevalence of radio afterglow emission by more than doubling the number of comprehensively modelled multi-wavelength afterglows, allowing for a sample analysis probing how the physical properties of GRB outflows evolve with time. In this paper, we present our first results: a 400-day observing campaign following the afterglow of GRB 230815A, which was the first afterglow detected through the program. In Section 2, we introduce the PanRadio GRB program and present the data obtained from our multi-wavelength observing campaign for GRB 230815A. In Section 3, we provide a description of the basic features we observe in the GRB 230815A afterglow. In Section 4, we provide a unified physical interpretation of the afterglow, make

inferences on the dynamical and microphysical evolution of the afterglow, and discuss the outlook for the broader PanRadio GRB program. We finally present our conclusions in Section 5.

Throughout this paper, we assume a flat  $\Lambda$ -CDM cosmology with  $H_0 = 69.6 \text{ km s}^{-1} \text{ Mpc}^{-1}$ ,  $\Omega_M = 0.286$ , and  $\Omega_\Lambda = 0.714$  (these were chosen to match cosmological parameters used in Duncan et al. (2023), which we compare some of our results in this manuscript with). We assume the following convention throughout, unless specified otherwise, for the temporal index  $\alpha$  and spectral index  $\beta$ :  $S(t, \nu) \propto t^\alpha \nu^\beta$ , where  $S(t, \nu)$  is the flux density as a function of time and frequency respectively. We further define here the X-ray photon index  $\Gamma$  to be related to the spectral index by  $\beta_x \equiv 1 - \Gamma$ . All errors are given at 68% confidence level.

## 2. OBSERVATIONS AND DATA REDUCTION

### 2.1. PanRadio GRB Program

The PanRadio GRB program on the Australia Telescope Compact Array (ATCA) began in April 2023. Through the program, we have and will continue to obtain high-cadence follow-up across a broad frequency range (1 – 50 GHz) for a large sample of *Swift*-localised GRBs observed over a period of at least three years, allowing us to build a more unbiased early- to late-time radio sample of GRBs. Ultimately, we will use this sample to improve our understanding of open questions relating to the dynamics and shock physics of GRBs, in particular, regarding: the composition and morphology of GRB jets; whether there is universality in some microphysical shock parameters among all GRBs as well as constraints on the evolution of these microphysical parameters as a function of time; and the implications of the inferred total energy budgets and environmental properties on the diversity of GRB progenitors.

A follow-up paper (Anderson et al., *in prep.*) will provide a complete description of the survey, the observing strategy, and initial sample analyses from bursts analysed in the first two years of the program. The remainder of this paper describes the 400-day observing campaign following the evolution of the afterglow for GRB 230815A; as the first afterglow detected through the PanRadio GRB program, we use it to highlight the potential science outcomes we can achieve with the entire sample following the completion of our program. Specifically, we will show through this campaign how the comprehensive early- to late-time follow-up of GRBs under the PanRadio GRB program can directly lead to insights into the electron acceleration processes, density profiles, and jet properties of the wider GRB population.

### 2.2. GRB 230815A Observing Campaign

GRB 230815A was detected by *Swift*/Burst Alert Telescope (BAT) at  $t_0 = 2023\text{-}08\text{-}15\text{T}10\text{:}49\text{:}55$  UT (Klingler et al. 2023). Although initially reported with a  $T_{90}$  duration of  $\sim 2$  s, the refined analysis in the 15 – 350 keV energy band was refined to  $17.00 \pm 7.62$  s (Laha et al. 2023). The GRB was also detected by the *Fermi*/Gamma-ray Burst Monitor (GBM) (Mailyan et al. 2023) and its  $T_{90}$  duration in the 50 – 300 keV band was 5.2 s, with the peak energy  $E_{\text{peak}} = 235 \pm 25$  keV in the time-averaged spectrum from  $t_0 + 0.002$  to  $t_0 + 3.264$  s from a fit with the Band function. The prompt emission properties suggest GRB 230815A is likely a standard long-soft GRB with a collapsar origin. The *Swift*/XRT identified the X-ray afterglow, localising it to RA (J2000)=12:18:53.34, Dec (J2000): -58:03:10.4, with a positional uncertainty of  $2''.2$  (Beardmore et al. 2023). The optical wavelengths were suppressed by considerable line-of-sight Galactic extinction, with a reddening of  $E(B - V) = 0.73$ , corresponding to a total visual extinction of  $A_V = 2.3$  for the typical Milky Way extinction-to-reddening ratio  $R_V = 3.1$  (Schlegel et al. 1998). This ultimately led to non-detections in all *Swift*/Ultra-violet Optical Telescope (UVOT) (Breeveld et al. 2023) and Southern Astrophysical Research (SOAR)/Goodman (Kilpatrick et al. 2023) filters, limiting follow-up with optical facilities and preventing a redshift determination.

At longer wavelengths, our team was able to detect and follow the evolution of the radio (Leung et al. 2023) and near-infrared (Schneider et al. 2023) afterglow with the ATCA and the Very Large Telescope High Acuity Wide-field *K*-band Imager (VLT/HAWK-I), respectively. We describe the observing campaign and the data reduction process for our radio and near-infrared observations below.

Our full set of measurements can be found in Tables 1 and 2. Table 1 shows the measurements from our radio observing campaign. Table 2 shows the optical and near-infrared measurements, including the upper limits acquired from the GCN Circulars as well as our near-infrared observing campaign. In this work, we used the *Swift*/XRT products, which were produced via the automated *Swift*/XRT analysis tools (Evans et al. 2009) and are publicly available through the UK *Swift* Science Data Centre.<sup>1</sup> The table of unabsorbed *Swift*/XRT fluxes at 0.3 – 10 keV was taken from the Swift Burst Analyser<sup>2</sup> (Evans et al. 2010); we consid-

<sup>1</sup> [https://www.swift.ac.uk/xrt\\_spectra/01185505/](https://www.swift.ac.uk/xrt_spectra/01185505/)

<sup>2</sup> [https://www.swift.ac.uk/burst\\_analyser/01185505/](https://www.swift.ac.uk/burst_analyser/01185505/)



ered data from the windowed timing (WT) and photon counting (PC) modes, but excluded all slewing data. The X-ray data was corrected for absorption, using  $N_{\text{H}} = 5.64 \times 10^{21} \text{ cm}^{-2}$  at  $z = 0$ , where  $N_{\text{H}}$  (Galactic) =  $4.94 \times 10^{21} \text{ cm}^{-2}$  and  $N_{\text{H}}$  (intrinsic) =  $0.7 \times 10^{21} \text{ cm}^{-2}$  as obtained from the late-time spectrum using photons from after 6 ks post-burst.

### 2.2.1. ATCA

We observed GRB 230815A under the PanRadio GRB program (PI: Anderson; C3542). Our first ATCA observations of GRB 230815A started at 02:00 UT on 2023 August 17 (or 1.6 days post-burst), leading to the discovery of the radio counterpart (Leung et al. 2023). We note that this GRB did not trigger the rapid-response capabilities of the telescope (which would carry out observations  $< 1$  day post-burst) because a message containing the *Swift*/BAT position was not circulated in the standard alerts stream, which was unusual<sup>3</sup> for events with a *Swift*/BAT detection. Since then, we collected an additional 11 epochs of data, with the final epoch occurring on 2024 September 24 (406 days post-burst).

Across the ATCA observing campaign, we used the 2.1, 5.5/9, 16.7/21.2, 33/35, and 43/45 GHz receiver configurations. We reduced the visibility data from each observation using standard MIRIAD procedures (Sault et al. 1995). We used B1934–638 to set the flux-density scale and B1129–58 to calibrate the time-variable complex gains. The singular exception is for the 9 GHz data obtained on 2024 June 13 UT, where the bootstrapping of the flux-density scale to B1934–638 failed; in this case, the flux-density scale was instead bootstrapped to B1129–58<sup>4</sup>, contributing to an additional uncertainty (of 15% from historical variability observed in the source) added in quadrature to the statistical uncertainties in the flux-density measurement. We also used B1934–638 to determine the bandpass response at the 2.1, 5.5, and 9 GHz frequency bands; at higher frequency bands (16.7 GHz and higher), we instead used B0727–115, B0537–441, or B1921–293, depending on which was higher in elevation at the start of our observing run. For observations at the higher frequency bands, we accounted for, to first order, the spectral shape of the bandpass calibrators (whose spectral shape is unknown unlike B1934–638) by fitting a flux-density model across the intermediate frequencies (e.g., 16.7 and 21.2 GHz).

<sup>3</sup> This has only occurred 15 times since the launch of *Swift*, see: [https://gcn.gsfc.nasa.gov/swift\\_grbs.html](https://gcn.gsfc.nasa.gov/swift_grbs.html)

<sup>4</sup> We are able to bootstrap the flux-density scale to B1129–58 because this source exhibits very limited variability at 9 GHz historically: [https://www.narrabri.atnf.csiro.au/calibrators/calibrator\\_database\\_viewcal?source=1129-58](https://www.narrabri.atnf.csiro.au/calibrators/calibrator_database_viewcal?source=1129-58)

After calibration, we imaged the visibilities data for the target field using the MIRIAD tasks INVERT, CLEAN, and RESTOR, with the multi-frequency synthesis CLEAN algorithm (Högbom 1974; Clark 1980; Sault & Wieringa 1994) used for deconvolution. The 2.1, 5.5, 9, 16.7, 21.2 GHz data were imaged using a 2 GHz bandwidth, while the higher frequency data (33/35 and 43/45 GHz) were imaged with a larger 4 GHz bandwidth by combining near-contiguous intermediate frequency bands to improve the image sensitivity. For each observation, we measure the flux density of a detected source by fitting a point-source model to the restored image using the MIRIAD task IMFIT and report a non-detection using the rms sensitivity obtained from the residual image. The errors reported are purely statistical, as the systematic errors are expected to be much smaller ( $\lesssim 5$  per cent; e.g., Reynolds 1994; Tingay et al. 2003). The final set of observation details and measurements are given in Table 1.

### 2.2.2. VLT/HAWK-I

We carried out observations of the GRB 230815A field with the 8.2 m Very Large Telescope (VLT) on Cerro Paranal (Chile). The observations were made with the HAWK-I near-infrared camera mounted on the Unit Telescope 4 (UT4, Yepun) in *H*-band at three epochs (0.52, 1.52, and 219.80 days post-burst) under the ESO program IDs 110.24CF.014 and 110.24CF.019 (PIs: N. Tanvir, D. Malesani, S. Vergani). The observations consisted of 20 min acquisitions (i.e., the total on-source exposure time without overhead) for the first two epochs and 36 min for the last epoch. All were obtained under excellent conditions (seeing  $< 0''.8$ ). The images were reduced using the standard European Southern Observatory (ESO) Reflex pipeline (Freudling et al. 2013) and the certified calibration files of the night provided by ESO. The photometric calibration was performed using nearby stars from the 2MASS catalogue (Skrutskie et al. 2006). We derived the magnitudes by aperture photometry using the ASTROPY PHOTUTILS package (v2.0.2, Bradley et al. 2024) and corrected for Galactic extinction using dust maps from Schlegel et al. (1998), which was accessed through <https://irsa.ipac.caltech.edu/applications/DUST/>.

In the first two epochs (0.52 and 1.52 days post-burst), two sources consistent with the XRT error circle were detected. One of them showed a clear sign of fading between the two epochs, from  $19.87 \pm 0.02$  to  $21.77 \pm 0.08$  AB magnitude (i.e., fading of  $\sim 2$  mag), confirming the variable nature of the source and was proposed as the near-infrared afterglow counterpart of the GRB (Schneider et al. 2023). A late-time observa-

**Table 1.** ATCA radio flux-density measurements for GRB 230815A. Columns 1 through 9 show the number of days since the *Swift*/BAT trigger (10:49:55 UT on 2023 August 15), the array configuration, and the flux-density measurements (or  $3\sigma$  limit for non-detections, where  $\sigma$  here is simply the rms noise) in  $\mu\text{Jy}$  at 2.1, 5.5, 9, 16.7, 21.2, 34, and 44 GHz.

dT (days)	Config	$S_{2.1\text{ GHz}}$	$S_{5.5\text{ GHz}}$	$S_{9\text{ GHz}}$	$S_{16.7\text{ GHz}}$	$S_{21.2\text{ GHz}}$	$S_{34\text{ GHz}}$	$S_{44\text{ GHz}}$
1.81	6D	—	$45 \pm 19$	$83 \pm 19$	$< 288$	$< 597$	—	—
3.63	6D	—	$49 \pm 17$	$76 \pm 16$	—	—	—	$168 \pm 38$
7.87	6D	—	$48 \pm 14$	$102 \pm 17$	—	—	—	—
9.60	6D	—	$< 39$	$79 \pm 15$	$210 \pm 25$	$223 \pm 41$	—	—
25.49	H168	—	$< 75$	$118 \pm 21$	$369 \pm 34$	$475 \pm 52$	—	—
39.46	H168	—	$< 93$	$175 \pm 23$	$502 \pm 45$	$598 \pm 58$	$410 \pm 57$	—
61.45	750B	—	$< 72$	$134 \pm 27$	$297 \pm 33$	$424 \pm 58$	$307 \pm 47$	—
96.45	H214	—	$< 84$	$< 99$	$313 \pm 86$	$< 498$	$< 636$	—
129.45	6D	$< 129$	$107 \pm 22$	$117 \pm 19$	$115 \pm 33$	$160 \pm 48$	—	—
212.99	6A	$< 108$	$< 57$	$112 \pm 18$	$84 \pm 24$	$< 174$	—	—
302.83	6D	—	$84 \pm 19$	$47 \pm 14$	$57 \pm 22$	$< 75$	—	—
405.77	6A	—	$80 \pm 17$	$49 \pm 9$	—	—	—	—

tion was obtained at 219.80 days post-burst to investigate possible host contamination in the early epochs. No clear source was detected at the afterglow position down to an AB magnitude of 24.2, confirming negligible host contamination in the first epochs. We provide the observational details and measurements in Table 2.

Using our VLT/HAWK-I detection at 0.52 days post-burst (corrected for Galactic extinction) along with *Swift* XRT photons from 0.464 days post-burst (at 1 keV), we assessed the optical darkness of GRB 230815A using the criterion outlined in van der Horst et al. (2009):  $\beta_{\text{ox}} < \beta_{\text{x}} - 0.5$ , where  $\beta_{\text{ox}}$  is the optical-to-X-ray spectral index,  $\beta_{\text{x}}$  is the X-ray spectral index, and here (only in this Section for consistency with the conventions in van der Horst et al. (2009)) the spectral index is defined as  $S_{\nu} \propto \nu^{-\beta}$ . We calculated  $\beta_{\text{ox}} = 0.74 \pm 0.03$  and, using the photon index from the PC segment of the spectrum  $\Gamma = 1.94^{+0.11}_{-0.10}$  (see Section 3.2), obtained  $\beta_{\text{x}} = 0.94^{+0.11}_{-0.10}$ . We therefore deem that it is very unlikely that GRB 230815A was a dark GRB and suggest instead that the majority of its optical suppression is due to Galactic extinction.

### 3. RESULTS

We report and characterise here the basic features of the afterglow identified from the X-ray, near-infrared, and radio observations.

#### 3.1. Break in the X-ray light curve

The first feature we identified from the X-ray light curve is an apparent break at approximately 10 ks post-burst as shown in Figure 1. We consider whether the presence of the break is significant (and quantify the pre/post-break decay slopes) by comparing a fit of the data to a smoothly broken power-law model:

$$S_t = S_{\text{break}} \left[ \frac{1}{2} \left( \frac{t}{t_b} \right)^{-s\delta_1} + \frac{1}{2} \left( \frac{t}{t_b} \right)^{-s\delta_2} \right]^{-1/s}, \quad (1)$$

where  $t$  is the time post-burst,  $S_t$  is the flux density as a function of time  $t$ ,  $\delta_1$  is the pre-break decay slope,  $\delta_2$  is the post-break decay slope,  $S_{\text{break}}$  and  $t_b$  are the approximate flux density and time post-burst corresponding to the break in the light curve, and  $s$  is the smoothness parameter; and a power-law model:

$$S_t = S_0 \left( \frac{t}{t_0} \right)^{\delta_1}, \quad (2)$$

where  $S_0$  is the normalisation parameter at time  $t_0 = 10$  ks assuming a decay with a power-law index of  $\delta_1$  without a break; under a Bayesian framework. Due to the higher density of data points at early times compared to later times, the data points were rebinned into 20 logarithmically spaced bins, shown with the red square markers in Figure 1, before fitting to minimise biases in sampling the posterior distribution.

**Table 2.** Optical and near-infrared measurements for GRB 230815A. Columns 1 through 8 show the number of days since the *Swift*/BAT trigger (10:49:55 UT on 2023 August 15), the observing instrument, photometric filter, the effective frequency corresponding to the photometric filter, the magnitude measurement, the magnitude measurement converted to a flux density, the magnitude measurement converted to a flux density *with* correction for Galactic extinction, and the reference where the measurement was obtained. Limits are derived by performing forced aperture photometry at the site of the source. The correction for Galactic extinction in the various filters is based on the dust maps from [Schlegel et al. \(1998\)](#), which was accessed through <https://irsa.ipac.caltech.edu/applications/DUST/>; for the *Swift*/UVOT filters, the extinction curves were determined using the values in [Roming et al. \(2009\)](#).

dT (days)	Instrument	Filter	$\nu$ (Hz)	Magnitude <i>uncorrected</i>	$S_\nu$ ( $\mu$ Jy) <i>uncorrected</i>	$S_\nu$ ( $\mu$ Jy) <i>corrected</i>	Ref
0.011	<i>Swift</i> /UVOT	v	5.54e+14	> 18.50	< 144.54	< 894.14	<a href="#">Breeveld et al. 2023</a>
0.011	<i>Swift</i> /UVOT	uvw2	1.44e+15	> 18.80	< 109.65	< 13711.08	""
0.012	<i>Swift</i> /UVOT	b	6.90e+14	> 19.30	< 69.18	< 766.97	""
0.012	<i>Swift</i> /UVOT	uvw1	1.12e+15	> 18.60	< 131.83	< 6529.31	""
0.014	<i>Swift</i> /UVOT	uvm2	1.34e+15	> 18.30	< 173.78	< 42761.16	""
0.039	<i>Swift</i> /UVOT	u	8.51e+14	> 19.40	< 63.10	< 1147.47	""
0.519	SOAR/Goodman	i	3.92e+14	> 20.50	< 22.91	< 72.44	<a href="#">Kilpatrick et al. 2023</a>
0.52	VLT/HAWK-I	H	1.87e+14	$20.19 \pm 0.02$	$30.48 \pm 0.56$	$41.65 \pm 0.77$	this work
0.542	SOAR/Goodman	z	3.09e+14	> 17.90	< 251.19	< 591.56	<a href="#">Kilpatrick et al. 2023</a>
1.52	VLT/HAWK-I	H	1.87e+14	$22.10 \pm 0.08$	$5.25 \pm 0.39$	$7.84 \pm 0.58$	this work
219.80	VLT/HAWK-I	H	1.87e+14	> 24.50	< 0.58	< 0.79	""

**Table 3.** The nested sampling best-fit parameters for the smoothly broken power-law (SBPL) and power-law (PL) models describing the *Swift*/XRT light curve at 1 keV for GRB 230815A. Column 1 shows the model used to fit the data, columns 2 through 6 show the best-fit parameters and their uncertainties for the model fits (i.e., the median and the 16<sup>th</sup>/84<sup>th</sup> percentile of the posterior distribution), column 7 shows the log evidence of the models, and column 8 shows the log Bayes factor comparing the SBPL and PL models.

	$S_{\text{break}}$ or $S_0$ ( $\mu$ Jy)	$t_b$ (s)	$\delta_1$	$\delta_2$	$s$	$\ln \mathcal{Z}$	$\ln \mathcal{B}_{\text{SBPL,PL}}$
SBPL	$2.60^{+1.53}_{-1.02}$	$10930^{+3175}_{-2575}$	$-1.26^{+0.05}_{-0.04}$	$-2.44^{+0.16}_{-0.19}$	$2.06^{+0.65}_{-0.77}$	-112.35	31.04
PL	$1.49^{+0.09}_{-0.08}$	—	$-1.57^{+0.02}_{-0.02}$	—	—	-143.39	

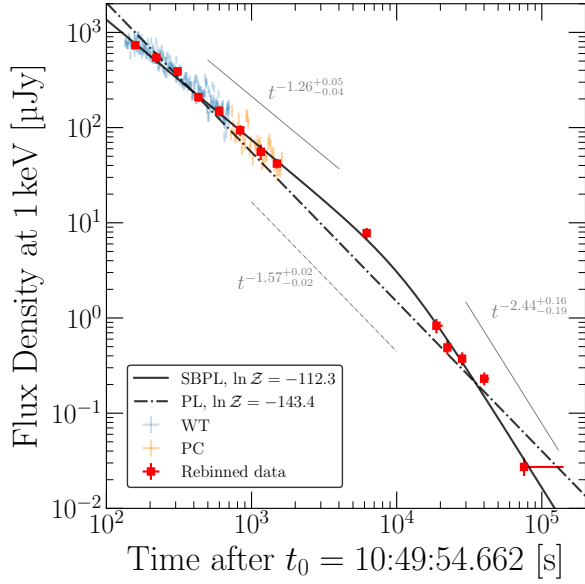


**Figure 1.** X-ray light curve for GRB 230815A. Data points obtained by the *Swift*/XRT in the WT mode are represented by blue error bars while those obtained in PC mode are represented by orange error bars. The data points used in the fits to the X-ray light curve, obtained from binning the *Swift*/XRT data points, are represented by red square markers. Fits to a smoothly broken power law and a power law are shown by the solid and dot-dashed lines, respectively. The slopes of the fits are annotated beside the lines.

We fit the rebinned data to both models using the nested sampler DYNESTY (Speagle 2020) as implemented in the Bayesian inferences software BILBY (Ash-ton et al. 2019). We performed the nested sampling using uniform priors (sampled uniformly over linear space), with 2 000 live points, and a stopping criterion on the change in the estimated Bayesian evidence  $\hat{Z}$  (i.e., the normalisation integral of the posterior probability function) from one iteration to the next of  $\Delta \ln(\hat{Z}) = 0.05$ . We show the nested sampling fits for the power-law and smoothly broken power-law models plotted on the X-ray light curve in Figure 1 as solid and dot-dashed lines, respectively; likewise, the fit for the smoothly broken power-law model is also plotted in the multi-wavelength light curve in Figure 3.

The resulting posterior distributions of the parameters in the fits of the X-ray light curve to both models are reported in Table 3 and are also shown in Figures 8 and 9 as corner plots. The logarithm of the Bayes factor comparing the smoothly broken power-law to the power-law model  $\ln \mathcal{B}_{\text{SBPL,PL}} = \ln \mathcal{Z}_{\text{SBPL}} - \ln \mathcal{Z}_{\text{PL}} = 31.04$ , where  $\mathcal{Z}_{\text{model}}$  is the Bayesian evidence for the data given the model, suggests the smoothly broken power law is the preferred model for explaining the X-ray data. The

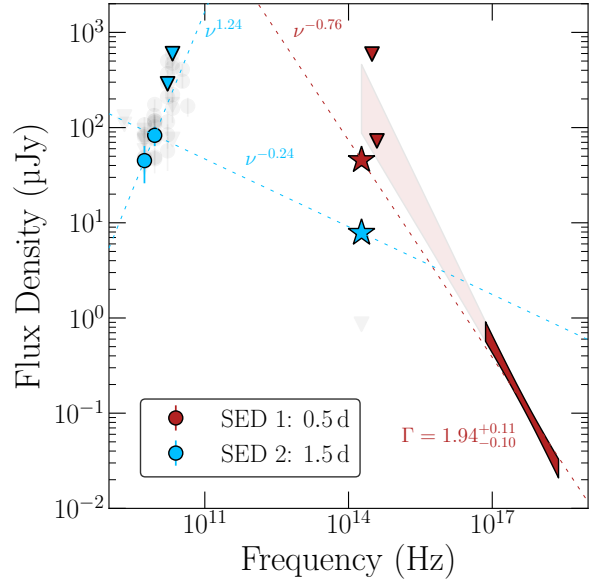


**Figure 2.** Broadband SED of GRB 230815A, showing two temporal snapshots at approximately 0.5 (red) and 1.5 (blue) days post-burst. The light gray points represent data from later epochs after 1.5 days post-burst. Radio detections are shown with circular markers, near-infrared detections with inverted triangular markers. The X-ray spectrum (dark red filled) is extrapolated to the near-infrared part of the spectrum (light red filled) using a photon index of  $\Gamma = 1.94^{+0.11}_{-0.10}$ , where the shaded region corresponds to a 68% confidence interval. The slopes between various data points in each spectral snapshot are annotated next to the corresponding dashed guide lines.

supported model indicates the presence of a break at  $t_b = 10.9^{+3.2}_{-2.6}$  ks post-burst with pre-break and post-break decays going as  $t^{-1.26^{+0.05}_{-0.04}}$  and  $t^{-2.44^{+0.16}_{-0.19}}$ , respectively.

### 3.2. Spectral break between the X-ray and near-infrared

Considering only the photons detected by the *Swift*/XRT while in PC mode, the overall time-averaged photon index was  $\Gamma(t_0 + 134 \text{ to } 45\,167 \text{ s}) = 1.94^{+0.11}_{-0.10}$ , where the mean photon arrival time was  $t_0 + 3\,322 \text{ s}$ . When considering the spectrum from the photons that were detected after the apparent X-ray light-curve break, the late-time time-averaged photon index was  $\Gamma(t_0 + 6\,081 \text{ to } 45\,167 \text{ s}) = 1.6^{+0.4}_{-0.3}$ , where the mean photon arrival time was  $t_0 + 21\,200 \text{ s}$ . Given the low photon count in this late-time segment, the uncertainties on the photon index are large, preventing us from determining whether the spectrum evolved after the apparent break.

In Figure 2 we plot the broadband spectral energy distribution (SED) of the GRB in two early snapshots at 0.5 and 1.5 days post-burst, where there is coverage across multiple windows of the broadband spec-



trum. The darker red shaded region shows the X-ray spectrum of the afterglow across the energy range of the *Swift*/XRT detector, using the measured unabsorbed flux from X-ray photons arriving approximately 0.5 days post-burst and assuming the aforementioned overall time-averaged photon index  $\Gamma = 1.94^{+0.11}_{-0.10}$  (i.e., assuming minimal evolution in the X-ray spectrum up until 0.5 days post-burst). In the lighter red shaded region, we extrapolated the X-ray spectrum beyond the detector energy range into the near-infrared part of the spectrum, where we were able to compare against the HAWK-I detection made at the same epoch. The near-infrared data point lies outside the shaded region of the extrapolated spectrum (corresponding to a 68% confidence interval), suggesting the possibility of a break between the X-ray and near-infrared bands at 0.5 days post-burst. Examining now the epoch at 1.5 days post-burst (corresponding to SED 2 coloured blue in Figure 2), the peak of the spectrum clearly lies between the radio and near-infrared wavelengths. The decay of the near-infrared spectrum from 0.5 to 1.5 days post-burst is also not as steep as the  $t^{-2.4 \pm 0.2}$  observed in the X-ray; instead, as shown more clearly in Figure 3 the decay follows a shallower  $t^{-1.6 \pm 0.1}$ .

### 3.3. Chromatic turnover in the radio light curves

The radio light curves at 5.5, 9, 16.7, and 21.2 GHz in Figure 3 show that they are evolving as smoothly broken power laws (as expected for a synchrotron afterglow) with indications of a chromatic break that occurs later for lower frequencies. Motivated by this, we fit a smoothly broken power-law function, given by Equation 1 (replacing  $S_{\text{break}}$  with  $S_{\text{peak}}$ ), to the light curves at each frequency, while setting the smoothness parameter to  $s = 3$  to reduce the degrees of freedom in the model (given the sparsity of data per frequency). Again, following the same nested sampling procedure described in Section 3.1, we fit all the light curves at once under two models with different assumptions. In the first model, we let the rise slope  $\delta_1$  and the decay slope  $\delta_2$  be independently sampled for each frequency. In the second model, motivated by the idea that the rise and decay slopes should be similar across all frequencies in the case that the evolution is caused by the passage of a characteristic frequency across the radio band, we fix the rise slope  $\delta_1$  and decay slope  $\delta_2$  to be common across different frequencies. We performed the nested sampling again using uniform priors, with 2000 live points, and a stopping criterion on the change in estimated evidence  $\hat{\mathcal{Z}}$  between iterations of  $\Delta \ln(\hat{\mathcal{Z}}) = 0.05$ .

The resulting posterior distributions of the parameters in the fits of the radio light curves to both models are

reported in Table 4 and are also shown in Figures 10 and 11 as corner plots. These show that in both models the break time and peak flux density for the light curve at 5.5 GHz are poorly constrained, suggesting that the light curve at this frequency may not have or has just recently turned over. Both models suggest the presence of a chromatic turnover in the radio light curves: at higher frequencies, the turnover occurs sooner with a higher peak flux density, which is consistent with what may be expected from a light-curve evolution that is due to a spectral break crossing the radio band as it moves towards lower frequencies (note this is applicable in certain configurations such as when  $\nu_m > \nu_a$  or in a stratified CBM, e.g., Gao et al. 2013).

The logarithm of the Bayes factor comparing model 1 (independent  $\delta_1$  and  $\delta_2$  per frequency) to model 2 (fixed  $\delta_1$  and  $\delta_2$  across all frequencies)  $\ln \mathcal{B}_{\text{model1,model2}} = \ln \mathcal{Z}_{\text{model1}} - \ln \mathcal{Z}_{\text{model2}} = 7.75$ , suggests that model 1 is better supported by the data than model 2. The key difference between the results from models 1 and 2 is that both the rise and decay slopes are steeper for higher frequencies when they are allowed to vary independently per frequency. As model 1 is better supported, these results indicate that the chromatic turnover cannot be attributed to just the passage of one characteristic frequency through the observing bands, but instead point to the possibility of two characteristic frequencies, namely  $\nu_a$  and  $\nu_m$ , passing through the observing bands with their ordering flipping at some point. The fit obtained for model 1 is plotted in the radio light curves in Figure 3, along with 50 randomly selected samples from the posterior parameter distribution (indicative of the fit uncertainty).

### 3.4. Radio chromatic evolution as described within the synchrotron paradigm

While our tests in the previous section show that the observed radio evolution is not well described by the passage of a single synchrotron break frequency through the bands, the spectral evolution (see Figure 4) clearly shows a transition from a regime where the lowest frequencies are self-absorbed (as suggested by the steeply rising spectral slope visible up to  $\sim 60$  days post-burst) to one where all frequencies lie on an optically thin branch of the spectrum. We therefore propose a more general scenario to describe the system, where two synchrotron frequencies – the injection frequency  $\nu_m$  and the self-absorption frequency  $\nu_a$  – cross the radio bands over the observed period, possibly also crossing each other. In order to obtain a description of the spectra and light curves that is always smooth, we opted for describing the optically thin synchrotron spectrum as a

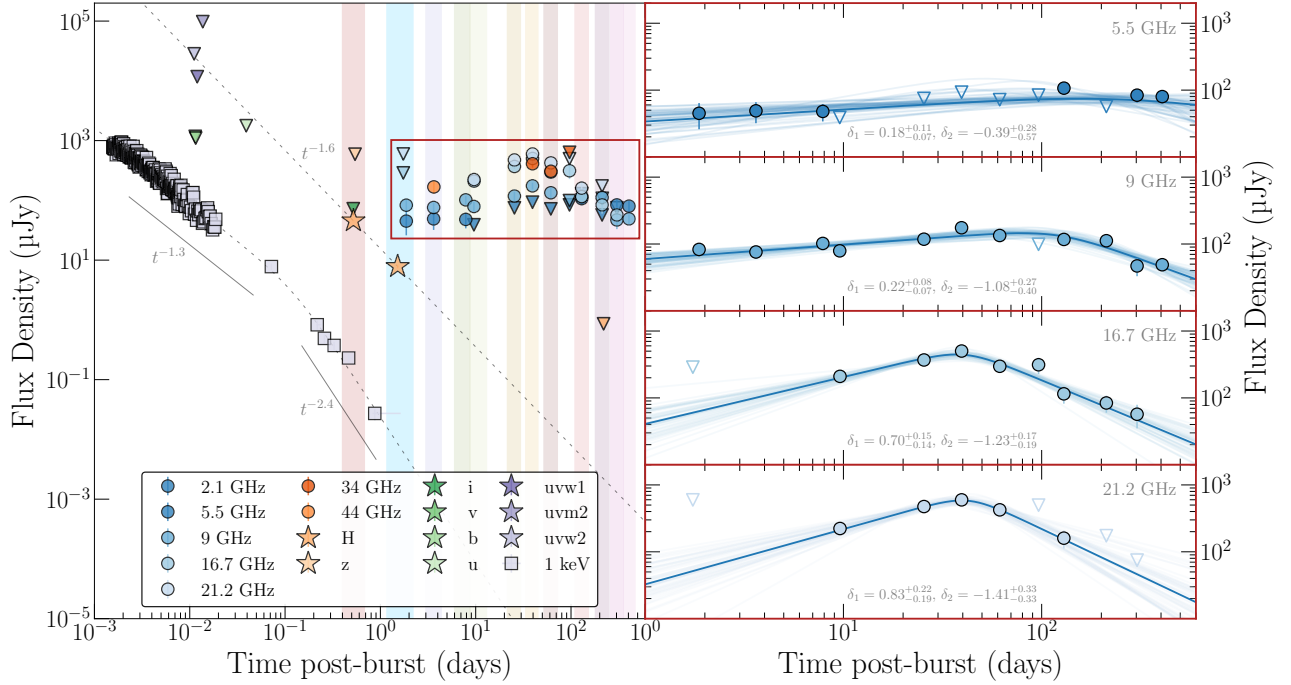


**Figure 3.** *Left:* Multi-wavelength light curves for GRB 230815A. The radio data points are represented with circular markers, the near-infrared data points with star markers, and the X-ray data points with square markers. All upper limits are shown with inverted triangular markers. The fits describing the evolution of the X-ray and near-infrared light curves are shown using dashed lines with the corresponding temporal slopes annotated next to them. The radio data points surrounded by the red rectangle are shown in more detail on the *right* panel. The coloured vertical strips indicate the temporal windows used for constructing the SEDs presented in Figures 2 and 4, where the colour of each strip here corresponds to an SED of the same colour in those Figures. *Right:* Radio light curves for GRB 230815A at 5.5, 9, 16.7, and 21.2 GHz (top to bottom). Each detection is represented by a circular marker and upper limit with an inverted triangular marker. At each frequency, the solid blue line represents the smoothly broken power-law fit (model 1; independent  $\delta_1$  and  $\delta_2$  per frequency) to the light curve using the best-fit parameters estimated from nested sampling, while the 50 lines with weaker line intensity are random posterior samples used to illustrate the fit uncertainties.

**Table 4.** The nested sampling best-fit parameters for two models describing the multi-frequency radio light curves for GRB 230815A at 5.5, 9, 16.7, and 21.2 GHz. The first model assumes the rise and decay slopes ( $\delta_1$  and  $\delta_2$ ) are independent for each frequency, while the second model fixes the rise and decay slopes to be the same for all frequencies. Column 1 shows the frequency, columns 2 through 5 show the best-fit parameters and their uncertainties for the model fits (i.e., the median and the 16<sup>th</sup>/84<sup>th</sup> percentile of the posterior distribution), column 6 shows the log evidence of the models, and column 7 shows the log Bayes factor comparing the two models.

Model 1: Independent $\delta_1, \delta_2$ per frequency						
	$S_{\text{peak}}$ ( $\mu\text{Jy}$ )	$t_{\text{b}}$ (days)	$\delta_1$	$\delta_2$	$\ln \mathcal{Z}$	$\ln \mathcal{B}_{\text{model1, model2}}$
5.5 GHz	$72.19^{+13.00}_{-9.68}$	$246.45^{+114.74}_{-156.43}$	$0.18^{+0.11}_{-0.07}$	$-0.37^{+0.27}_{-0.52}$	$-173.67$	$7.75$
9 GHz	$134.90^{+17.87}_{-16.77}$	$119.68^{+47.59}_{-36.13}$	$0.22^{+0.08}_{-0.07}$	$-1.09^{+0.28}_{-0.40}$		
16.7 GHz	$440.10^{+33.25}_{-32.70}$	$40.80^{+4.85}_{-4.50}$	$0.70^{+0.15}_{-0.13}$	$-1.23^{+0.16}_{-0.19}$		
21.2 GHz	$580.30^{+48.43}_{-48.68}$	$42.76^{+5.97}_{-6.13}$	$0.82^{+0.21}_{-0.18}$	$-1.42^{+0.33}_{-0.33}$		
Model 2: Common $\delta_1, \delta_2$ across different frequencies						
	$S_{\text{peak}}$ ( $\mu\text{Jy}$ )	$t_{\text{b}}$ (days)	$\delta_1$	$\delta_2$	$\ln \mathcal{Z}$	$\ln \mathcal{B}_{\text{model1, model2}}$
5.5 GHz	$105.05^{+32.17}_{-26.13}$	$134.52^{+181.47}_{-44.46}$	$0.39^{+0.08}_{-0.08}$	$-1.14^{+0.13}_{-0.15}$	$-181.42$	$7.75$
9 GHz	$171.11^{+16.05}_{-16.28}$	$93.71^{+20.16}_{-15.98}$				
16.7 GHz	$368.18^{+25.49}_{-25.15}$	$47.83^{+6.60}_{-5.56}$				
21.2 GHz	$468.27^{+36.82}_{-34.61}$	$51.63^{+7.75}_{-6.40}$				

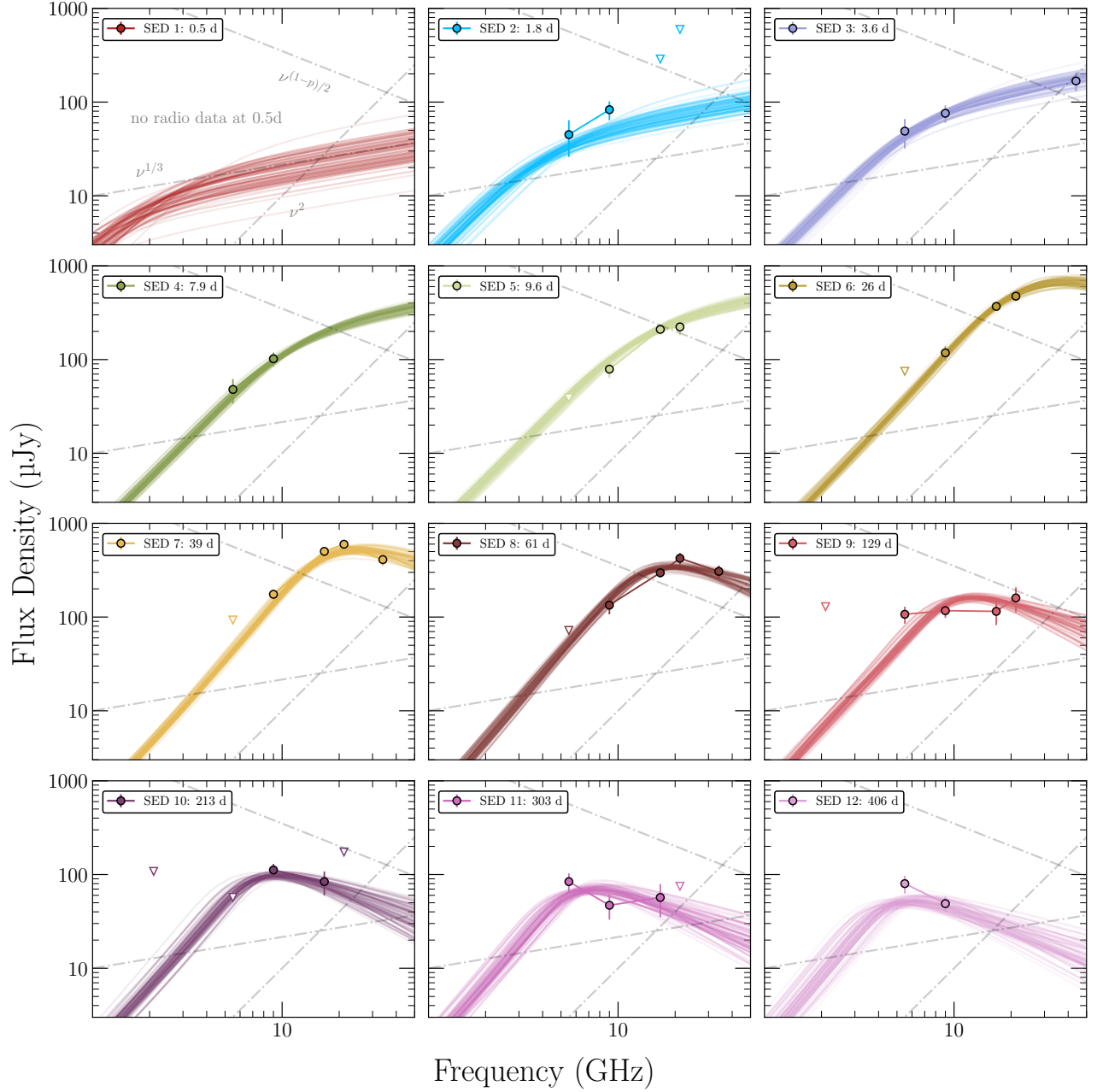


**Figure 4.** Radio SEDs of GRB 230815A at the 12 different epochs constructed from the temporal windows shown in Figure 3. The epoch is labelled in the legend for each panel. The dot-dashed lines are guide lines showing different spectral slopes. These spectral slopes are labelled in SED 1 (0.5 days post-burst) with  $p = 2.2$  adopted here (see text). Detections are shown in filled circular markers while  $3\sigma$  upper limits for non-detections are shown using inverted triangular markers. The thin lines in each panel show model spectra from 100 random posterior samples from the nested sampling procedure performed to constrain our evolving synchrotron model in Subsection 3.4.

smoothly-broken power law:

$$S_{\nu,\text{thin}} = S_{\nu_m} \left[ \left( \frac{\nu}{\nu_m} \right)^{-s_1/3} + \left( \frac{\nu}{\nu_m} \right)^{s_1(p-1)/2} \right]^{-1/s_1}, \quad (3)$$

where  $S_{\nu_m}$  is the flux density at the extrapolated meeting point of the two power law branches (Granot & Sari 2002), and  $s_1$  is a smoothing parameter; the frequency-dependent synchrotron self-absorption optical depth as (see e.g., Panaitescu & Kumar 2000):

$$\tau_{\nu,\text{SSA}} = \tau_{\nu_m} \left[ \left( \frac{\nu}{\nu_m} \right)^{s_2 5/3} + \left( \frac{\nu}{\nu_m} \right)^{s_2(p+4)/2} \right]^{-1/s_2}, \quad (4)$$

where  $\tau_{\nu_m}$  is the optical depth at  $\nu_m$ , and  $s_2$  is another smoothing parameter. From basic radiative transfer (assuming the emitting and absorbing electron populations to be the same), the resulting spectrum is then

$$S_\nu = S_{\nu,\text{thin}} \frac{1 - \exp(-\tau_{\nu,\text{SSA}})}{\tau_{\nu,\text{SSA}}}. \quad (5)$$

The benefit of this description over the more widely adopted Granot & Sari (2002) one is that it does not suffer from a discontinuous behavior when  $\nu_m$  and  $\nu_a$  cross each other.

For what concerns the time evolution of the spectral parameters  $S_{\nu_m}$ ,  $\tau_{\nu_m}$  and  $\nu_m$ , we opted for a simple description in terms of power laws, namely:

$$S_{\nu_m}(t) = S_{\nu_m,0} \left( \frac{t}{t_0} \right)^{\alpha_S}, \quad (6)$$

$$\tau_{\nu_m}(t) = \tau_{\nu_m,0} \left( \frac{t}{t_0} \right)^{\alpha_\tau}, \quad (7)$$

$$\nu_m(t) = \nu_{m,0} \left( \frac{t}{t_0} \right)^{\alpha_m}, \quad (8)$$

where we chose the reference time to be  $t_0 = 100$  days. The resulting model has 9 parameters, namely  $s_1$ ,  $s_2$ ,  $S_{\nu_m,0}$ ,  $\tau_{\nu_m,0}$ ,  $\nu_{m,0}$ ,  $\alpha_S$ ,  $\alpha_\tau$ ,  $\alpha_m$ , and  $p$ . We estimated the posterior probability distributions of these parameters adopting the same nested sampling technique as in previous sections, assuming relatively wide and uninformative priors as detailed in Table 5, where we also report summaries of the fit results. The full corner plot is shown in Figure 12 in the Appendix. The thin lines in each panel of Figure 4 show model spectra from 100 random posterior samples, demonstrating that the model successfully reproduces the observed evolution.

The temporal evolution of the break frequencies  $\nu_m$  and  $\nu_a$  (defined as the frequency for which  $\tau_{\nu,\text{SSA}} = 1$ ) implied by the model is shown in Figure 5. The dash-dotted grey lines in the figure show the expected evolution for a Blandford & McKee (1976) blast wave with

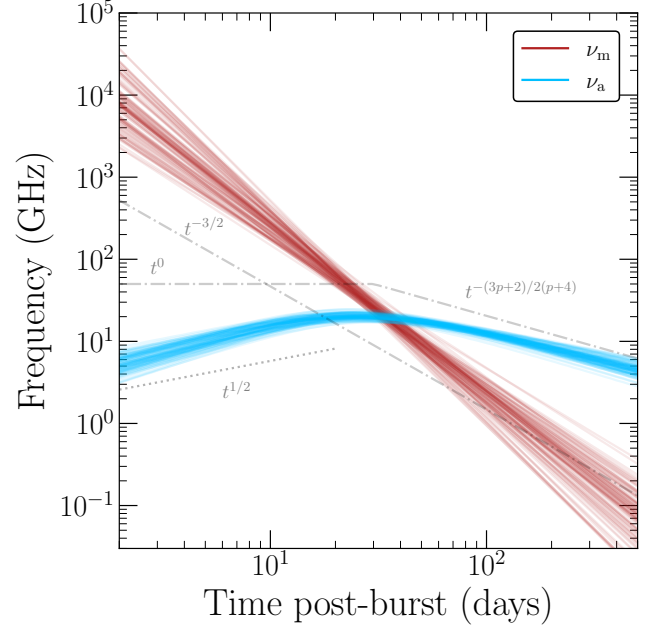


**Figure 5.** Time evolution of the injection ( $\nu_m$ , red lines) and self-absorption ( $\nu_a$ , blue lines) frequencies from 100 random posterior samples of the evolving synchrotron spectrum model of Subsection 3.4. The grey dash-dotted lines show the expected evolution of the two frequencies in the self-similar phase of a Blandford & McKee (1976) blast wave (valid for an homogenous ISM environment), as given in Granot & Sari (2002), assuming  $p = 2.6$ . The dotted line shows  $t^{1/2}$ , which approximates the initial evolution of  $\nu_a$ .

constant microphysical parameters (Granot & Sari 2002, where the  $\nu_m$  evolution is valid for both ISM and wind, while that of  $\nu_a$  is shown only for the ISM case here), where  $t^0$  (resp.  $t^{-(3p+2)/2(p+4)}$ ) refers to the evolution of  $\nu_a$  prior to (resp. after) being crossed by  $\nu_m$ . The  $\nu_m$  evolution preferred by the model is somewhat steeper than the expected one ( $\alpha_m \sim -2.1 \pm 0.3$  instead of the expected  $-1.5$ ); the evolution of  $\nu_a$  is slightly increasing before the  $\nu_m$  crossing (approximately as  $t^{1/2}$ , instead of the expected  $t^0$ ), and it is somewhat shallower than the expected one after the crossing. In addition, the result shows a mild preference for a slightly increasing  $S_{\nu_m}$ , quantitatively  $\alpha_S \sim 0.2 \pm 0.13$ , in contrast with the expected constant (ISM) or slowly decreasing (wind) behaviour (Granot & Sari 2002). In general, the non-standard evolution of the shock dynamics from the standard self-similar expansion (e.g., energy injection, sideways expansion) or an evolution of the microphysical parameters. We note that a very similar result is found in an analogous analysis of late-time radio observations of GRB 241025A (Giarratana et al., *in preparation*), pos-



**Table 5.** Nested sampling results for the evolving self-absorbed synchrotron spectrum model of Subsection 3.4. Below each parameter we report the support of the prior (uniform for all parameters in the reported range) and a summary of the result, which consists in the median and 68% symmetric credible interval of the marginalised posterior probability of that parameter. The full corner plot is shown in Figure 12.

Parameter	$s_1$	$s_2$	$\log(S_{\nu_{m,0}}/\mu\text{Jy})$	$\log(\tau_{\nu_{m,0}})$	$\log(\nu_{m,0}/\text{GHz})$	$\alpha_S$	$\alpha_\tau$	$\alpha_m$	$p$
Prior range	[0.5, 3]	[0.5, 3]	[1, 6]	[-3, 6]	[-3, 3]	[-4, 0.5]	[0, 6]	[-4, 4]	[2.01, 4]
Result	$2.63^{+0.26}_{-0.43}$	$0.58^{+0.10}_{-0.06}$	$3.10^{+0.10}_{-0.09}$	$2.67^{+0.37}_{-0.37}$	$0.32^{+0.16}_{-0.17}$	$0.19^{+0.13}_{-0.12}$	$4.71^{+0.56}_{-0.51}$	$-2.12^{+0.26}_{-0.29}$	$2.57^{+0.41}_{-0.33}$

sibly pointing to a widespread behaviour among GRB radio afterglows.

#### 4. DISCUSSION

##### 4.1. A Unified Physical Picture of GRB 230815A

The X-ray break (Subsection 3.1) at  $10.9^{+3.2}_{-2.6}$  ks (or  $0.13^{+0.04}_{-0.03}$  days) post-burst transitions from a pre-break temporal slope of  $\delta_1 = -1.26^{+0.05}_{-0.04}$  to a post-break temporal slope of  $\delta_2 = -2.44^{+0.16}_{-0.19}$ . This change in temporal slope after the break  $\Delta\delta = |\delta_2 - \delta_1| = 1.18^{+0.24}_{-0.20}$  cannot be explained by the passing of the cooling break  $\nu_c$  through the X-ray band since this is expected to yield  $\Delta\delta = 1/4$  in both the homogeneous and stellar wind scenarios (e.g., Granot & Sari 2002). To strengthen this point, if the break was due to the passing of  $\nu_c$ , for any given value of the electron spectral index  $p$  (defined as the power-law index of the synchrotron electron energy distribution  $\frac{dN}{dE} \propto E^{-p}$ ), the steepest resulting temporal slope should go as  $\propto t^{\frac{1-3p}{4}}$ , which would still require a very extreme  $p \approx 3.5$  (e.g., Wang et al. 2015) inconsistent with the values inferred from the photon index (discussed below). Instead, we propose that the break observed in the X-ray is an early jet break. Analytical solutions for the jet break, considering the edge effect and lateral spreading, suggest the slopes of the temporal decay in both the homogeneous and stellar-wind environment can be as steep as  $\propto t^{-p}$  (in the  $\nu > \nu_m$  and  $\nu > \nu_c > \nu_m$  spectral regimes; Rhoads 1999; Sari et al. 1999; Livio & Waxman 2000); however, when considering only the edge effect with no lateral spreading, there will be a more shallow change of  $3/4$  (resp.  $1/2$ ) in the temporal index with respect to the pre-break slope in the homogeneous (resp. wind) environment (e.g., Gao et al. 2013). A more detailed numerical study of the jet break in the homogeneous density CBM environment yields a post-jet break decay index of  $0.28 - 1.29p$  for an on-axis observer of a jet with typical opening angle  $0.1\text{rad}$  in the  $\nu > \nu_c$  spectral regime (van Eerten & MacFadyen 2013); this constrains the electron spectral index to  $p = 2.11^{+0.15}_{-0.12}$ . While a similar numerical study comprehensively quantifying the pre- and post-jet break behaviour is not available for a stratified CBM environment, other studies have indicated that the post-break decay slope in a stellar-wind environment is expected to

be similar or shallower by up to a factor of  $\sim 2/3$  (e.g., see figure 10 in De Colle et al. 2012), allowing for a steeper yet physical  $p \sim 2.6$ .

We then consider the measured X-ray photon index (see Subsection 3.2) of  $\Gamma = 1.94^{+0.11}_{-0.10}$ , which implies a spectral index of  $\beta_x = -0.94^{+0.10}_{-0.11}$ . We can obtain an estimate of  $p$  using standard closure relations (e.g., Sari et al. 1998) by considering the possibilities of whether the X-ray band  $\nu_x$  is located below or above  $\nu_c$ . In the scenario that  $\nu_x < \nu_c$ , the spectral index goes as  $S_\nu \propto \nu^{\frac{1-p}{2}}$ , so the spectral index  $\beta_x$  implies  $p = 2.88^{+0.22}_{-0.20}$ , which is inconsistent with the lower  $p$  estimated from the post-jet break temporal index in a homogeneous environment, but possibly consistent with the steeper estimate in the stellar-wind environment (quoted above). However, the expected pre-jet break temporal index in a stellar-wind environment goes as  $\propto t^{\frac{1-3p}{4}}$  so the  $p = 2.88^{+0.22}_{-0.20}$  inferred from the spectral index would imply a temporal index of  $-1.91^{+0.15}_{-0.17}$ , which is too steep to explain the much shallower pre-jet break decay of  $-1.26^{+0.05}_{-0.04}$ . Therefore, it is unlikely that  $\nu_x < \nu_c$  at 0.5 days post-burst; indeed, in Figure 2 the X-ray spectrum extrapolated to the near-infrared suggests that it is possible (at  $>1\sigma$  confidence) that the near-infrared and X-ray data points do not lie on the same spectral segment. In the scenario  $\nu_c < \nu_x$ , the spectral index goes as  $S_\nu \propto \nu^{-\frac{p}{2}}$ , implying a lower estimate for  $p = 1.88^{+0.22}_{-0.20}$ , while the pre-jet break temporal indices go as  $\propto t^{\frac{2-3p}{4}}$  in both the homogeneous and stellar-wind CBM environment, yielding an estimate of  $p = 2.35^{+0.05}_{-0.07}$ , consistent at 90%-confidence level to the estimate from the spectral index. We note that the tendency towards lower values of  $p$  inferred here gives preference to the homogeneous environment over the stellar-wind environment. Using this information and adopting  $p = 2.2$ , taken as the middle point between the two estimates of  $p$  from the X-ray temporal and spectral indices, respectively, and that  $\nu_o < \nu_c < \nu_x$ , we estimate the cooling break at the epoch of  $\sim 0.5$  days to be a  $\sim 10^{16}$  Hz with the flux density at the break to be  $\sim 1\mu\text{Jy}$ .

After the jet break, the decay of the near-infrared slope as  $t^{-1.6 \pm 0.1}$  (see Subsection 3.2) is shallower than the post-break slope observed in the X-ray decaying as  $t^{-2.4 \pm 0.2}$ . If the X-ray and near-infrared bands are ob-

serving radiation from the same emitting component, their post-jet break decay slopes should match, since the predicted decay slopes should be similar in both the spectral regimes of  $\nu_c > \nu > \nu_m$  and  $\nu > \nu_c > \nu_m$  for both the analytical (e.g., [Sari et al. 1999](#)) and numerical (e.g., [van Eerten & MacFadyen 2013](#)) predictions that consider lateral spreading. Without considering lateral spreading (and just the edge effect), the difference in the temporal decay in the  $\nu_c > \nu > \nu_m$  and  $\nu > \nu_c > \nu_m$  spectral segments should differ by 1/4 (e.g., [Gao et al. 2013](#)), which is insufficient to explain the difference of  $0.8 \pm 0.2$  observed between the post-jet break X-ray and near-infrared decay slopes. The presence of a flatter slope at the near-infrared wavelengths could indicate an additional component; due to the limited spectral and temporal coverage around this time and wavelength, it is difficult to constrain the properties and origins of this excess, e.g., whether it may be related to the origins of the radio emission (discussed below) or something else.

We next consider the radio light curves (Subsection 3.3) and the evolving SEDs (Subsection 3.4). The chromatic turnover in the radio light curves is indicative of the passing of a (or multiple) characteristic synchrotron frequency (frequencies) through the observing band. The lack of any observed achromatic breaks in the radio light curves suggests that even at 400 days post-burst, there is no evidence for changes to a new dynamical regime, such as a transition into the non-relativistic regime or into a different surrounding density profile. Most surprisingly, the decays of the radio light curves (which are all  $\gtrsim -1.42$ ) are much shallower than that observed in the X-ray following the jet break; if the X-ray and radio afterglow emission share the same origins, their post-jet break decay slopes (after the spectral peak  $\max(\nu_m, \nu_a)$  passes through the band) should be the same. Furthermore, in the post-jet break scenario considering both the edge effect and lateral spreading, the light curves are expected to decay according to power laws in all synchrotron spectral segments (for both the homogeneous and stellar wind scenarios, as  $t^{-p}$  at  $\nu > \nu_m$  and  $\nu > \nu_c > \nu_m$ , as  $t^{-1/3}$  at  $\nu_a < \nu < \nu_m$ , and as  $t^0$  at  $\nu < \nu_a$ ; e.g., [Sari et al. 1999](#); [Livio & Waxman 2000](#)), which is in contrast to the rising light curves observed at each radio frequency. However, if lateral spreading is not considered to be significant until much later and only the edge effect is considered (e.g., see [Gao et al. 2013](#), and references therein), there is only one scenario (in the  $\nu_a < \nu_m$  configuration that is applicable to our rising radio light curves, see Figure 5) where an increasing light curve is possible: i.e., in the spectral regime of  $\nu < \nu_a$  in a stellar wind environment the light curve is predicted to go as  $t^{1/2}$ . Even then, our data is

incompatible with this picture for the post-jet break radio behaviour in three ways: (i) the 21.2 GHz light curve should be in the  $\nu_a < \nu < \nu_m$  spectral segment which should be decreasing as  $t^{-1/2}$  unlike the  $\nu < \nu_a$  segment, (ii) after  $\max(\nu_a, \nu_m)$  passes the observing band the light curve should decrease according to  $t^{-(3p+1)/4 \approx -2}$  compared to the  $t^{-1.42}$  (and shallower) we observe in our light curves after their turnovers, and (iii) it is far more likely (as discussed in the subsequent paragraphs) that the GRB exploded in a homogeneous ISM and not wind environment. The observed radio behaviour is therefore difficult to reconcile with the jet break observed in the X-ray data.

This suggests the radio emission comes from a different emission origin to that of the X-rays. We summarise the key features of the observed radio emission as follows: (1) chromatic turnover in the radio light curves with an earlier turnover and higher peak flux density at higher frequencies; (2) temporal rise and decay indices for the radio light curves of approximately  $0.4^{+0.1}_{-0.1}$  and  $-1.1^{+0.1}_{-0.2}$ , respectively, with both the rise and decay being sharper at higher frequencies, suggesting the passage and crossing of both  $\nu_a$  and  $\nu_m$  across the observing band; (3) the radio spectrum is initially self-absorbed and then evolves to an optically-thin slope of  $(1-p)/2$ , where  $p = 2.57^{+0.41}_{-0.33}$ , with the passage of both  $\nu_a$  and  $\nu_m$  through the observing band and  $\nu_a$  crossing  $\nu_m$  at approximately  $\sim 20$  GHz and  $\sim 50$  days post-burst; (4)  $\nu_a$  evolves approximately as  $\nu_a \propto t^{1/2}$  prior to crossing  $\nu_m$  (this is closer to the  $\nu_a \propto t^0$  expected in the homogeneous scenario than the  $\nu_a \propto t^{-3/5}$  expected in the wind scenario) and shallower than the temporal evolution of  $t^{-(3p+2)/2(p+4)}$  expected for a [Blandford & McKee \(1976\)](#) blast wave with constant microphysical parameters after crossing  $\nu_m$  in both the homogeneous and wind scenario (e.g., [Granot & Sari 2002](#)); and (5)  $\nu_m$  evolves as  $\nu_m \propto t^{-2.1 \pm 0.3}$ , which is steeper than the decay of  $\nu_m \propto t^{-1.5}$  expected in both the homogeneous and wind scenarios, while  $S_{\nu_m}$  evolves as  $S_{\nu_m} \propto t^{0.2 \pm 0.13}$ , which is slightly increasing and is more consistent with the expected constant ISM behaviour compared with the slowly decreasing  $S_{\nu_m} \propto t^{-1/2}$  expected in the wind environment (e.g., [Granot & Sari 2002](#)).

As previously mentioned, these radio afterglow properties display minor deviations away from the standard shock dynamics expected from the standard self-similar expansion (e.g., [Granot & Sari 2002](#)), which could be indicative of additional energy injection, multi-component jet structure, sideways expansion, or an evolution of the microphysical parameters. Nevertheless, as shown in the aforementioned points (4) and (5), the properties are more consistent with expanding into a homogeneous

density environment than a stellar wind environment. We note here that while the  $p = 2.57^{+0.41}_{-0.33}$  in point (3) is slightly higher than the  $p \approx 2.2$  determined earlier from the X-ray data, they are broadly consistent with each other since the uncertainties on  $p$  from the evolving radio synchrotron model in Subsection 3.4 are larger given that the optically thin spectrum is relatively unconstrained by the data; we further note that the optically thin SEDs 10 and 11 in Figure 4 have a slope of approximately  $-0.6$ , which is consistent with  $p \approx 2.2$ . Critically, we inferred from these radio light curves that the blast wave evolution is inconsistent with the post-jet break scenario, which is in direct conflict with the jet break observed in the X-ray light curve, because: (i) the radio decay slopes are much shallower than the post-jet break decay slope in the X-ray light curve when they should be similar post jet-break even if they are in different spectral segments; (ii) the observed rising radio light curve is not consistent with what is expected in the post-jet break scenario (see prior discussion about the expected light curve behaviour in the post-jet break scenario when considering both the scenario with and without lateral spreading); and (iii) the expected decay of  $S_{\nu_m} \propto t^{-1}$  in the post-jet break scenario is inconsistent with the slightly positive increase we see in  $S_{\nu_m}$  as a function of time (Sari et al. 1999; Livio & Waxman 2000; van Eerten & MacFadyen 2013; Gao et al. 2013).

There are two options to reconcile this: the jet break at radio frequencies is delayed with respect to the X-ray band, or the structure of the jet is different to the standard top-hat model. In the former scenario, it is possible that the jet break at radio frequencies could be delayed with respect to the X-ray band, simply because the radio-emitting electrons are located in regions of the outflow further away from the jet edge (which is tracked better by the high-energy X-ray electrons) due to limb brightening and self-absorption effects (van Eerten et al. 2011). However, these effects would typically delay the jet break by a factor of a few or up to an order of magnitude (e.g., van Eerten et al. 2011; De Colle et al. 2012), which is insufficient to explain the greater than two orders of magnitude delay in jet break time we see between the X-ray and radio light curves for GRB 230815A, thus disfavouring this scenario. We propose instead that the remaining option to reconcile this involves a two-component jet (e.g., Berger et al. 2003; Starling et al. 2005; Racusin et al. 2008; van der Horst et al. 2014): a fast, narrow component responsible for the early X-ray jet break, and a slower, wide component responsible for the delayed (or lack of) jet break observed at radio frequencies even at 400 days post-burst. Comprehensive modelling of the multi-wavelength light

curves using a two-component jet model (where the dynamics of the two jets are coupled together, rather than independent as assumed in this manuscript) can verify this and characterise the components of the system, but this is beyond the scope of this work. We stress that for any future multi-wavelength modelling pursuits, the lack of a redshift measurement and the unconstrained location of the cooling break corresponding to the second wider component will lead to large uncertainties in constraining the outflow physical parameters.

We note that in order to more clearly highlight the features of the afterglow in this picture we invoked the two-component jet. However, it is more likely that the two-component jet is a simplified approximation for a more realistic structured jet, which has a continuous (rather than with two distinct components) angular stratification in its kinetic energy (see, e.g., Lamb et al. 2021; Salafia & Ghirlanda 2022).

#### 4.2. Inferred Dynamical and Microphysical Properties

Even without a redshift measurement and standard multi-wavelength afterglow modelling, light curves and broadband spectral snapshots enable us to make some inferences on the dynamical and microphysical properties of the GRB that would otherwise not be possible without a comprehensive, high-cadence follow-up of the radio afterglow.

##### 4.2.1. Jet Geometry

Starting with the X-ray jet break, we can constrain the half-opening angle of the narrow jet component (e.g., Sari et al. 1999; Zhang & MacFadyen 2009):

$$\theta_j = 2.1^\circ \left( \frac{t_j}{0.1 \text{ days}} \right)^{3/8} \left( \frac{1+z}{1+1.5} \right)^{-3/8} \cdot \left( \frac{E_{\text{kin,iso}}}{10^{53} \text{ erg}} \right)^{-1/8} \left( \frac{n_0}{1 \text{ cm}^{-3}} \right)^{1/8}, \quad (9)$$

where  $t_j$  is the jet break time in days post-burst in the observer frame,  $z$  is the redshift,<sup>5</sup>  $E_{\text{kin,iso}}$  is the isotropic-equivalent kinetic energy of the outflow,<sup>6</sup> and  $n_0$  is the

<sup>5</sup> Redshift is assumed here to be  $z = 1.5$ , noting that the median inferred redshift for GRBs is approximately  $z \approx 1.7$  based on the sample found at <https://www.mpe.mpg.de/~jcg/grbgen.html> compiled by Jochen Greiner

<sup>6</sup> We estimate  $E_{\text{kin,iso}}$  by assuming a prompt efficiency  $\epsilon_\gamma = E_{\gamma,\text{iso}} / (E_{\gamma,\text{iso}} + E_{\text{kin,iso}} + E_{\text{kin,iso,w}}) = 15\%$  (e.g., Beniamini et al. 2016). Here,  $E_{\gamma,\text{iso}} \approx \frac{4\pi d_L^2}{(1+z)} S_\gamma$ , where  $d_L$  is the luminosity distance assuming  $z = 1.5$ ,  $S_\gamma = 1.28 \pm 0.01 \text{ erg cm}^{-2}$  is the fluence detected by the *Fermi*/GBM across the energy band 10–1000 keV (Mailyan et al. 2023), and  $E_{\text{kin,iso,w}}$  is the isotropic-equivalent kinetic energy from the wider component. This yields  $E_{\text{kin,iso}} + E_{\text{kin,iso,w}} \approx 4 \times 10^{53} \text{ erg}$ , so we estimate within an order of magnitude  $E_{\text{kin,iso}} = 10^{53} \text{ erg}$ .

density of the CBM environment. The early jet break implies a very narrow jet opening angle, consistent with the narrow end of the long GRB distribution (Ryan et al. 2015; Wang et al. 2018), but inconsistent with the distribution of short GRB jet opening angles inferred from previous sample studies (Fong et al. 2015). If we now consider the wider component responsible for the radio emission in the two-component jet scenario, we can constrain how much wider the jet opening angle is for this component  $\theta_{j,w}$  (compared to the narrow component) as a function of the wider component's jet break time  $t_{j,w}$ , which is at least greater than 400 days post-burst, and isotropic-equivalent kinetic energy  $E_{\text{kin,iso,w}}$ , which we varied from 1/10 to 10 times that of the narrower component  $E_{\text{kin,iso}}$ . Precisely how much of the kinetic energy is in the wider component depends then on its formation, which is uncertain (and hence why the allowable range for  $E_{\text{kin,iso,w}}$  was varied over 3 orders of magnitude) – e.g., if it is interpreted as a cocoon then it depends on how efficiently the energy can be deposited as the jet head propagates through the vestiges of the stellar envelope (Matzner 2003; Bromberg et al. 2011; Salafia & Ghirlanda 2022). Our constraints are shown in Figure 6. We find that in all scenarios the half-opening angle of the wider component should exceed  $35^\circ$  (assuming the same redshift and CBM density as in Equation 9). The ratio comparing the half-opening angle of the wider component to the narrow component is:

$$\frac{\theta_{j,w}}{\theta_j} \approx 17 \left( \frac{t_{j,w}}{400 \text{ days}} \right)^{3/8} \left( \frac{E_{\text{kin,iso,w}}/E_{\text{kin,iso}}}{10} \right)^{-1/8}, \quad (10)$$

or equivalently,  $\theta_{j,w} \gtrsim 17 \theta_j$ . For comparison, previous GRBs that invoke a two-component jet to explain their afterglow emission have a wide range of narrow and wide component half-opening angles: e.g., GRB 030329 has larger half-opening angles of  $\theta_j = 5^\circ$  and  $\theta_{j,w} = 17^\circ$  (Berger et al. 2003), while GRB 080319B has smaller half-opening angles of  $\theta_j = 0.2^\circ$  and  $\theta_{j,w} = 5^\circ$  (Racusin et al. 2008).

#### 4.2.2. (Lack of) Non-relativistic Transition

The 400-day afterglow also reveals no change to a new dynamical regime, such as approaching a different CBM density profile or transitioning into the non-relativistic regime, since there is no evidence for any achromatic breaks in the multi-frequency light curves. We first note that the GRB properties are consistent with exploding in a homogeneous environment, inferred from as early as the X-ray data. This homogeneous environment could be indicative of (i) the part of the stellar wind that has been compressed by the reverse shock from the wind's interaction with the ISM, or (ii) a wind termination-

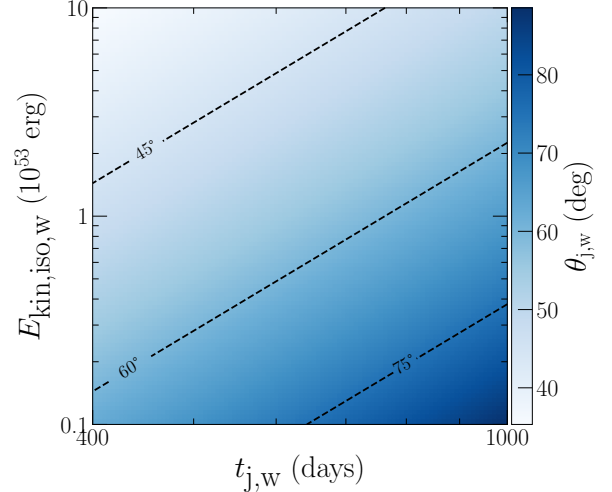


**Figure 6.** Half-opening angle of the wider component  $\theta_{j,w}$  (in degrees) as a function of the jet break  $t_{j,w}$  (days) and isotropic-equivalent kinetic energy  $E_{k,iso,w}$  (erg). The dashed lines indicate the combination of  $t_{j,w}$  and  $E_{k,iso,w}$  that will yield a  $\theta_{j,w}$  of  $45^\circ$ ,  $60^\circ$ , and  $75^\circ$ . We assume here the redshift and CBM density from Equation 9, effectively performing a relative scaling from the  $2.1^\circ$  narrow jet.

shock radius that is located quite close to the progenitor such as in the case where the CBM environment is dense or the stellar wind has low momentum (Ramirez-Ruiz et al. 2005).

The lack of observed achromatic break also means the blast wave has not entered the non-relativistic regime, which often happens at time:

$$t_{\text{NR}} \approx 425 \left( \frac{1+z}{1+1.5} \right) \left( \frac{E_{\text{kin,iso,w}}}{10^{53} \text{ erg}} \right)^{1/3} \left( \frac{n_0}{1 \text{ cm}^{-3}} \right)^{-1/3} \text{ days}, \quad (11)$$

where the time of the non-relativistic transition is given in the observer frame (e.g., Piran 2004; Zhang & MacFadyen 2009; Barniol Duran & Giannios 2015). From this equation, a very typical time for the transition would be approximately 400 days post-burst, which is consistent with the lack of a clear transition observed after 400 days post-burst for GRB 230815A (here we assume in the equation a similar isotropic-equivalent kinetic energy for the narrow and wide jet components, both approximately  $10^{53}$  erg). This indicates that, where possible, a GRB should be followed many years post-burst to probe the physical evolution of GRBs in this regime. In certain configurations – e.g., bursts with substantially lower than typical kinetic energies or higher densities – the non-relativistic transition occurs much earlier, making the follow-up requirements are less stringent; for GRB 970508  $t_{\text{NR}} \approx 100$  days (Frail et al. 2000) and for GRB 030329  $t_{\text{NR}} \approx 50$  days (Frail et al.



2005; Resmi et al. 2005; van der Horst et al. 2005). After the transition to the non-relativistic regime at  $t_{\text{NR}}$ , the blast wave can be described with the Sedov-von Neumann-Taylor self-similar solution and results in a flattening of the light curve (Frail et al. 2000; Zhang & MacFadyen 2009; Sironi & Giannios 2013). The transition is smooth, making it difficult to pinpoint the light curve break, but after the transition accurate calorimetric measurements can be made without degeneracy from the jet geometry.

While we cannot make these calorimetric measurements for GRB 230815A since it has not clearly entered the non-relativistic regime, we can use Equation 11 to constrain the ratio between the blast wave kinetic energy and the CBM density. This ratio determines the Sedov length (Blandford & McKee 1976) –  $l_S \equiv \left( \frac{E_{\text{kin,iso,w}}}{\frac{4}{3}\pi n_0 m_p c^2} \right)^{1/3}$ , where  $m_p$  is the proton mass and  $c$  is the speed of light – which is the fundamental length scale governing the expansion of the blast wave, e.g., from which the radius and expansion speed of the blast wave can be determined (e.g., Barniol Duran & Giannios 2015; Granot et al. 2018, and references therein). With  $t_{\text{NR}} > 400$  days (and Equation 11), we constrain the ratio between the blast wave kinetic energy and the CBM density to be:

$$\log[(E_{\text{kin,iso,w}}/n_0)/\text{erg cm}^3] > 54.1 - 3\log(1+z). \quad (12)$$

This gives us  $\log[(E_{\text{kin,iso,w}}/n_0)/\text{erg cm}^3] > 52.9$  if we take  $z = 1.5$  as before, which disfavors particularly low blast-wave kinetic energies and high CBM densities.

#### 4.2.3. Universality in Electron Acceleration Processes

Even without multi-wavelength modelling of the afterglow due to the aforementioned difficulties, we can still gain valuable insights into the microphysical evolution of the afterglow by tracing the synchrotron peak at radio frequencies (Beniamini & van der Horst 2017; Duncan et al. 2023). In particular, we assume that the turnover of the light curves at the radio frequencies is due to the passage of  $\nu_m$  across the observing frequency and obtain measurements of the time and flux density of the radio synchrotron peak at four different frequencies (as shown in Table 4). With this, we can evaluate the parameter  $\Psi$ , which relates the observed radio peaks to a set of microphysical parameters, effectively acting as a proxy for  $\epsilon_e$ , the fractional shock energy in the electrons (Beniamini & van der Horst 2017; Duncan et al. 2023). In the homogeneous ISM environment, this relation is

given by:

$$\Psi_{\text{ism}} = \left( \frac{261.4(1+z)^{1/2} \nu_p^{3/2} E_{\gamma,\text{iso},53}^{1/2}}{10^{15} d_{28}^2 S_{\nu_p} \max(1, t_p/t_j)^{1/2}} \right)^{1/2} \quad (13)$$

$$= \frac{p-2}{0.177(p-1)} \left( \frac{p-0.67}{p+0.14} \right)^{1/2} \left( \frac{1-\epsilon_\gamma}{\epsilon_\gamma} \right)^{-1/4} \cdot n_0^{-1/4} \epsilon_e \xi_e^{-3/2}, \quad (14)$$

where  $\nu_p$  is the peak frequency in Hz<sup>7</sup>,  $t_p$  is the peak time in days,  $S_{\nu_p}$  is the peak flux density in mJy,  $E_{\gamma,\text{iso}} = 10^{53} E_{\gamma,\text{iso},53}$  erg is the isotropic-equivalent energy released from the high-energy prompt emission,  $d_{28}$  is the luminosity distance to the GRB in units of  $10^{28}$  cm,  $\epsilon_\gamma = E_{\gamma,\text{iso}}/(E_{\gamma,\text{iso}} + E_{\text{kin,iso}})$  is the energy efficiency of the prompt emission, and  $\xi_e$  is the fraction of electrons that are accelerated by the shock into the synchrotron power-law distribution.

The derived value for the parameter  $\Psi$  can then be used to evaluate the parameter  $\chi$  (Duncan et al. 2023), which effectively acts as a proxy for  $\gamma_m$ , the minimum Lorentz factor of the electron spectral distribution (corresponding to the synchrotron injection frequency). In the homogeneous ISM environment, this is given by the relation:

$$\chi_{\text{ism}} = 266 \Psi_{\text{ism}} E_{\gamma,\text{iso},53}^{1/8} (1+z)^{3/8} t_d^{-3/8} \quad (15)$$

$$= \left( \frac{p-0.67}{0.66(p+0.14)} \right)^{1/2} \left( \frac{\epsilon_\gamma}{1-\epsilon_\gamma} \right)^{3/8} \cdot n_0^{-1/8} \gamma_m \xi_e^{-1/2}, \quad (16)$$

where  $t_d$  is the time post-burst in days.

As discussed in Subsection 4.1, we inferred GRB 230815A to be exploding in a homogeneous ISM environment. However, for completeness, we also evaluate these parameters for the stellar wind environment. The relation for  $\Psi_{\text{wind}}$  is given by:

$$\Psi_{\text{wind}} = \left( \frac{249.4(1+z) \nu_p t_p}{10^{15} d_{28}^2 S_{\nu_p}} \right)^{1/2} \quad (17)$$

$$= \frac{p-2}{0.277(p-1)} \left( \frac{p-0.69}{p+0.12} \right)^{1/2} A_*^{-1/2} \epsilon_e \xi_e^{-3/2}, \quad (18)$$

where  $A_*$  is a parameter related to the normalisation of the density profile in a wind environment. In the stellar wind environment, the density is expected to fall as  $n(r) = Ar^{-2}$ , where  $A$  is related to the mass-loss rate

<sup>7</sup> The units for this was mistakenly stated as GHz in Duncan et al. (2023)

$\dot{M}_w$  and the progenitor's stellar wind velocity  $v_w$  by  $A = \dot{M}_w / 4\pi v_w = 5 \times 10^{11} A_* \text{ g cm}^{-1}$ . We set  $A_*$  to return the normalisation of  $A$ , such that  $A_* = 1$  represents a typical Wolf-Rayet star with  $\dot{M}_w = 10^{-5} M_\odot \text{ yr}^{-1}$  and  $v_w = 1000 \text{ km s}^{-1}$ . Similarly, the relation for  $\chi_{\text{wind}}$  is given by:

$$\chi_{\text{wind}} = 475 \Psi_{\text{wind}} E_{\gamma, \text{iso}, 53}^{1/4} (1+z)^{1/4} t_d^{-1/4} \quad (19)$$

$$= \left( \frac{p - 0.69}{0.65(p + 0.12)} \right)^{1/2} \left( \frac{\epsilon_\gamma}{1 - \epsilon_\gamma} \right)^{1/4} \cdot A_*^{-1/4} \gamma_m \xi_e^{-1/2}. \quad (20)$$

The evaluated values of  $\Psi$  and  $\chi$  are given in Table 6 and also shown in Figure 7. We note here that  $\chi$  is evaluated at  $t_d = 1$  day to compare with the distributions found in Duncan et al. (2023). The *left* and *middle* panels of the figure show measurements of each parameter with their uncertainties at each frequency in both the homogeneous ISM (both assuming and not assuming the presence of a jet break at 0.1 days post-burst) and stellar wind environments. These measurements are compared against the GRB population distribution determined from the Duncan et al. (2023) sample, with the  $1\sigma$  confidence interval on these parameters shaded in blue (for the ISM environment) and orange (for the stellar wind environment). The *right* panel of the figure then shows the evolution of  $\Psi$  as a function of time in days post-burst for GRB 230815A.

We find that both the  $\Psi$  and  $\chi$  values are most consistent with the distributions found in the Duncan et al. (2023) sample if we assume an ISM environment and a jet break at 0.1 days corresponding to the X-ray jet break (see Figure 7 *left* and *middle* panels). However, we stress that this analysis alone does not rule out an ISM environment with no jet break nor a wind environment. This is because if we consider 16.7 and 21.2 GHz only, the parameter values in all three scenarios lie within the known distributions in the Duncan et al. (2023) sample (even if it is not within the  $1\sigma$  spread around the mean). As discussed in Duncan et al. (2023), the variations in these distributions can be almost completely explained by the typical variations in the CBM density, supporting the idea of a narrow distribution (or possibly universal values) for the microphysical parameters related to the electron acceleration process, i.e.,  $\epsilon_e$  and  $\gamma_m$ .

In Figure 7 (*right* panel), it is clear that there appears to be an evolution of the parameter  $\Psi$  (and consequently also  $\chi$ ) over time. However, in our evolving synchrotron model for our radio SEDs reported in Subsection 3.4, it is clear  $\nu_m$  crosses  $\nu_a$  at  $\sim 50$  days post-burst (see Figure 5). In this scenario (when  $\nu_a > \nu_m$  and the blast wave starting to become sub-relativistic, *not*

non-relativistic), the assumptions in Equations 13 to 20 break down and therefore we cannot interpret the increasing values of  $\Psi$  with time as evidence for evolution in the microphysical parameters with time. For the same reason, we only considered 16.7 and 21.2 GHz above in the interpretation of the  $\Psi$  and  $\chi$  parameters in the context of their known distributions.

Future tests of the universality or constraints on the evolution of electron acceleration processes would benefit significantly from comprehensive observations (high-cadence and long follow-up campaign) over more frequencies (ideally above the typical self-absorption frequency of the afterglow). Deviations from the known distributions may point to extreme microphysical properties and provide observational evidence supporting microphysical parameters being time-variable. These insights are also independent of any broadband modelling, making them free from biases and variations from different modelling methodologies, while requiring significantly less multi-wavelength data and computational resources.

#### 4.3. The need for a more complete and unbiased survey of radio afterglows

GRB 230815A would likely not have been followed at radio frequencies without the PanRadio GRB Program and even more unlikely to be followed more than a year post-burst. This is because radio follow-up has often been prioritised and biased towards GRBs where comprehensive multi-wavelength coverage is available (Chandra & Frail 2012). Given the high line-of-sight extinction for this event, optical coverage was sparse and a redshift determination was not available (so it would likely not have been prioritised for radio follow-up).

Still, even without comprehensive multi-wavelength coverage, it is clear that the multi-frequency radio light curves provided valuable insights into the system. As discussed in Subsection 4.2, they were critical for providing insights into the density profile of the CBM environment, the nature of the jet structure and geometry, and constraints on dynamical and microphysical processes (in this case, the transition into the non-relativistic regime and universality of microphysical parameters describing electron acceleration processes). Future events would provide even more insight if: (a) they were also triggered under the rapid-response mode (on source in  $< 24$  hr); (b) there was an even longer temporal baseline, which would be possible with more sensitive next-generation radio telescopes, to probe the non-relativistic transition and perform calorimetric measurements; and (c) there was a redshift, which would enable a more

**Table 6.** The  $\Psi$  and  $\chi$  values calculated for GRB 230815A at the observing frequencies of 5.5, 9, 16.7, and 21.2 GHz using the turnovers in their light curves (given in parentheses), assuming they are due to the passage of  $\nu_m$ . In the table are 3 sets of  $\Psi$  and  $\chi$  values: from left to right are the values assuming an ISM environment with the jet break occurring at 0.1 days post-burst (corresponding to the X-ray jet break); an ISM environment with the jet break at 1000 days (corresponding to the lack of jet break observed for the radio light curves assuming a two-component model); and a stellar wind environment.

	$\Psi_{\text{ism, jet break}}$	$\chi_{\text{ism, jet break}}$	$\Psi_{\text{ism, no jet break}}$	$\chi_{\text{ism, no jet break}}$	$\Psi_{\text{wind}}$	$\chi_{\text{wind}}$
5.5 GHz ( $241 \pm 151$ days)	$0.45 \pm 0.15$	$170 \pm 60$	$3.2 \pm 1.5$	$1200 \pm 600$	$0.99 \pm 0.32$	$590 \pm 190$
9.0 GHz ( $121 \pm 47$ days)	$0.30 \pm 0.06$	$113 \pm 23$	$1.8 \pm 0.5$	$660 \pm 200$	$0.66 \pm 0.13$	$390 \pm 80$
16.7 GHz ( $41 \pm 5$ days)	$0.13 \pm 0.01$	$49 \pm 3$	$0.59 \pm 0.06$	$220 \pm 20$	$0.29 \pm 0.02$	$170 \pm 10$
21.2 GHz ( $41 \pm 6$ days)	$0.13 \pm 0.01$	$50 \pm 4$	$0.60 \pm 0.07$	$230 \pm 30$	$0.29 \pm 0.02$	$170 \pm 10$

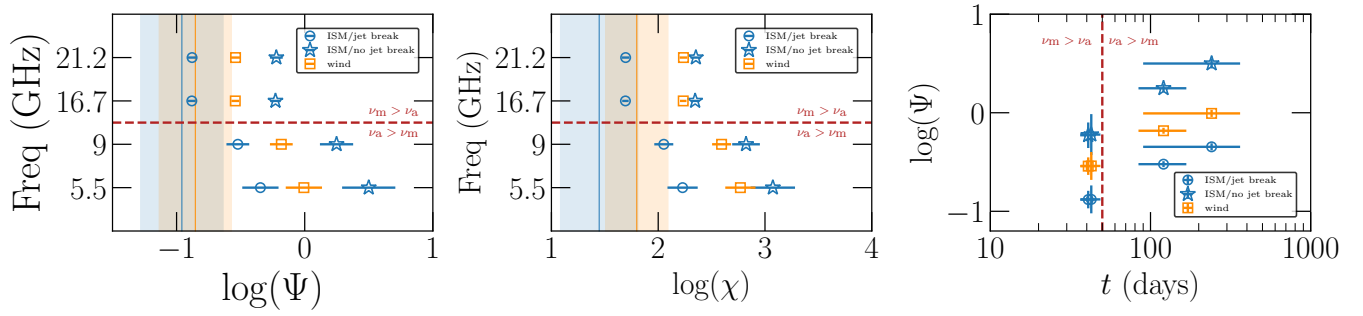


**Figure 7.** *Left:* Values for  $\log(\Psi)$  for GRB 230815A as determined from the light-curve turnovers at 5.5, 9, 16.7, and 21.2 GHz. *Middle:* Values for  $\log(\chi)$  for GRB 230815A as determined from the light-curve turnovers at 5.5, 9, 16.7, and 21.2 GHz. *Right:* Values for  $\log(\Psi)$  for GRB 230815A as a function of time in days post-burst. For each panel, blue circular markers are used for measurements that assume an ISM environment and a jet break at 0.1 days post-burst (corresponding to the X-ray jet break), blue star markers are used for measurements that assume an ISM environment and no jet break yet at 400 days post-burst (corresponding to the observed radio behaviour), and the orange square markers are used for measurements that assume a stellar wind environment. For the *left* and *middle* panels, the shaded regions correspond to the  $1\sigma$  confidence intervals centred on the weighted average (solid vertical line) of  $\Psi$  and  $\chi$  values, respectively, for the Duncan et al. (2023) sample in the ISM (blue) and stellar wind (orange) environment. The red dashed line in each panel represents where  $\nu_m$  passes  $\nu_a$  (see Subsection 3.4); this is likely responsible for the apparent evolution in the parameters.

rigorous modelling of the system and inferences on the physical properties with smaller uncertainties.

Clearly, a complete understanding of the diversity in the GRB population and its properties would require an unbiased and comprehensive survey of radio afterglows. The PanRadio GRB Program will extend this work to a large sample of GRBs, providing a survey of all southern *Swift*-detected GRBs, following these events regardless of a detected multi-wavelength counterpart, line-of-sight extinction, or redshift measurement, etc. This will then provide a more unbiased view of GRB property distributions, including phenomenological properties such as the radio brightness distribution and physical properties such as the jet structure. The larger and more unbiased sample of GRBs will also provide a better chance to follow more GRBs up to very late times. We should therefore be able to constrain many more GRBs through their

transition to the non-relativistic regime, where calorimetric measurements can be made with minimal degeneracy with other jet parameters such as the jet geometry. Additionally, we will be able to see how common a delayed jet break is at radio frequencies, whether they can be attributed to the radio-emitting electrons being further away from the jet edge, and gain a better understanding of what determines the wind termination-shock radius. Currently the primary hindrance in our understanding of these is low-sample statistics; the PanRadio GRB program aims to improve this. A full description of the survey, the observing strategy, and initial sample analyses from bursts analysed in the first two years of the program will be provided in our follow-up paper (Anderson et al., *in prep.*).

## 5. CONCLUSIONS

GRB 230815A was the first radio afterglow to be followed from early through to very late times under the PanRadio GRB program. Our observing campaign for GRB 230815A lasted more than 400 days, including dedicated follow-up from the VLT/HAWK-I and the ATCA. Further optical and spectroscopic follow-up to attain a redshift, however, was limited due to the high line-of-sight extinction with  $A_V = 2.3$ . We found that the early X-ray jet break at  $\sim 0.1$  days post-burst was inconsistent with the evolution of the multi-frequency radio light curves, which were approximately evolving (with some minor deviations discussed in Subsection 4.1) in accordance with the standard shock dynamics expected from the Blandford & McKee (1976) self-similar expansion into a homogeneous ISM environment prior to a jet break. One option we propose to reconcile these features is to invoke a two-component jet: the early X-ray break originates from a very narrow component with half-opening angle  $\sim 2.1^\circ$ , while the observed evolution of the radio light curves stems from a wider component with half-opening angle  $\gtrsim 35^\circ$ .

Throughout the 400-day campaign, we did not find any evidence suggesting a change in the CBM density profile or a transition to the non-relativistic regime. The lack of transition into the non-relativistic regime at 400 days post-burst constrains the ratio between the blast wave kinetic energy and the CBM density to  $\log[(E_{\text{kin,iso}}/n_0)/\text{erg cm}^3] > 52.9$  (assuming a GRB redshift of  $z = 1.5$  like before), which disfavors particularly low blast-wave kinetic energies and high CBM densities. By tracing the evolution of the afterglow in multiple frequencies, we were also able to put some constraints on the evolution of the microphysical shock parameters describing the electron acceleration processes; in particular we do not find any evidence supporting an evolution in these parameters with time nor any significant deviation in these parameters from their distributions derived from a wider sample of GRBs.

Many of the insights revealed about GRB 230815A were only possible through a multi-frequency, high-cadence campaign up to very late times about 400 days post-burst. The PanRadio GRB program – a systematic, multi-year, radio survey of all southern *Swift* GRB events, tracing the multi-frequency evolution of their afterglows from within an hour to years post-burst, conducted using the ATCA – will extend these insights from single events to a comprehensive sample level. It is then through the sample analysis that we will answer many of the remaining questions about long GRBs and the diversity of events within this subpopulation, from their jet structure/geometry, environments, energetics, to their dynamical and microphysical evolution.

## ACKNOWLEDGMENTS

JKL acknowledges support from the University of Toronto and Hebrew University of Jerusalem through the University of Toronto - Hebrew University of Jerusalem Research and Training Alliance program. The Dunlap Institute is funded through an endowment established by the David Dunlap family and the University of Toronto. BS acknowledges the support of the French Agence Nationale de la Recherche (ANR), under grant ANR-23-CE31-0011 (project PEGaSUS). FDC acknowledges support from the UNAM-PAPIIT grant IN113424. AJG is grateful for support from the Forrest Research Foundation. BPG acknowledges support from STFC grant No. ST/Y002253/1 and The Leverhulme Trust grant No. RPG-2024-117. FS acknowledges the support of the French Agence Nationale de la Recherche (ANR), under grant ANR-22-CE31-0012 (project MOTS). RLCS acknowledges support from The Leverhulme Trust grant RPG-2023-240. NRT acknowledges support from STFC grant ST/W000857/1. Part of this research was supported by the Australian Research Council Centre of Excellence for Gravitational Wave Discovery (OzGrav), project number CE230100016. The Australia Telescope Compact Array is part of the Australia Telescope National Facility (<https://ror.org/05qajvd42>) which is funded by the Australian Government for operation as a National Facility managed by CSIRO. We acknowledge the Gomeroi people as the Traditional Owners of the Observatory site. Based on observations collected at the European Southern Observatory under ESO programmes 110.24CF.014 and 110.24CF.019. This work made use of data supplied by the UK Swift Science Data Centre at the University of Leicester. This research made use of PHOTOUTILS, an ASTROPY package for detection and photometry of astronomical sources (Bradley et al. 2024).

*Facilities:* ATCA, *Swift* (XRT and UVOT), SOAR/Goodman, VLT/HAWK-I

*Software:* ASTROPY (Astropy Collaboration et al. 2013, 2018), BILBY (Ashton et al. 2019), DYNesty (Speagle 2020), MATPLOTLIB (Hunter 2007), NUMPY (Harris et al. 2020), PANDAS (McKinney 2010), PHOTOUTILS (Bradley et al. 2024), SCIPY (Virtanen et al. 2020), and MIRIAD (Sault et al. 1995).



## REFERENCES

- Abdalla, H., Adam, R., Aharonian, F., et al. 2019, *Nature*, 575, 464, doi: [10.1038/s41586-019-1743-9](https://doi.org/10.1038/s41586-019-1743-9)
- Anderson, G. E., van der Horst, A. J., Staley, T. D., et al. 2014, *MNRAS*, 440, 2059, doi: [10.1093/mnras/stu478](https://doi.org/10.1093/mnras/stu478)
- Anderson, G. E., Staley, T. D., van der Horst, A. J., et al. 2018, *MNRAS*, 473, 1512, doi: [10.1093/mnras/stx2407](https://doi.org/10.1093/mnras/stx2407)
- Ashton, G., Hübner, M., Lasky, P. D., et al. 2019, *ApJS*, 241, 27, doi: [10.3847/1538-4365/ab06fc](https://doi.org/10.3847/1538-4365/ab06fc)
- Astropy Collaboration, Robitaille, T. P., Tollerud, E. J., et al. 2013, *A&A*, 558, A33, doi: [10.1051/0004-6361/201322068](https://doi.org/10.1051/0004-6361/201322068)
- Astropy Collaboration, Price-Whelan, A. M., SipHocz, B. M., et al. 2018, 156, 123, doi: [10.3847/1538-3881/aabc4f](https://doi.org/10.3847/1538-3881/aabc4f)
- Barniol Duran, R., & Giannios, D. 2015, *MNRAS*, 454, 1711, doi: [10.1093/mnras/stv2004](https://doi.org/10.1093/mnras/stv2004)
- Beardmore, A. P., Evans, P. A., Goad, M. R., Osborne, J. P., & Swift-XRT Team. 2023, *GRB Coordinates Network*, 34437, 1
- Beniamini, P., Nava, L., & Piran, T. 2016, *MNRAS*, 461, 51, doi: [10.1093/mnras/stw1331](https://doi.org/10.1093/mnras/stw1331)
- Beniamini, P., & van der Horst, A. J. 2017, *MNRAS*, 472, 3161, doi: [10.1093/mnras/stx2203](https://doi.org/10.1093/mnras/stx2203)
- Berger, E., Diercks, A., Frail, D. A., et al. 2001, *ApJ*, 556, 556, doi: [10.1086/321612](https://doi.org/10.1086/321612)
- Berger, E., Kulkarni, S. R., Pooley, G., et al. 2003, *Nature*, 426, 154, doi: [10.1038/nature01998](https://doi.org/10.1038/nature01998)
- Blandford, R. D., & McKee, C. F. 1976, *Physics of Fluids*, 19, 1130, doi: [10.1063/1.861619](https://doi.org/10.1063/1.861619)
- Bradley, L., Sipőcz, B., Robitaille, T., et al. 2024, *astropy/photutils: 2.0.2*, Zenodo, doi: [10.5281/zenodo.13989456](https://doi.org/10.5281/zenodo.13989456)
- Breeveld, A. A., Klingler, N. J., & Swift/UVOT Team. 2023, *GRB Coordinates Network*, 34446, 1
- Bright, J. S., Rhodes, L., Farah, W., et al. 2023, *Nature Astronomy*, 7, 986, doi: [10.1038/s41550-023-01997-9](https://doi.org/10.1038/s41550-023-01997-9)
- Bromberg, O., Nakar, E., Piran, T., & Sari, R. 2011, *ApJ*, 740, 100, doi: [10.1088/0004-637X/740/2/100](https://doi.org/10.1088/0004-637X/740/2/100)
- Chandra, P., & Frail, D. A. 2012, *ApJ*, 746, 156, doi: [10.1088/0004-637X/746/2/156](https://doi.org/10.1088/0004-637X/746/2/156)
- Chrimes, A. A., Gompertz, B. P., Kann, D. A., et al. 2022, *MNRAS*, 515, 2591, doi: [10.1093/mnras/stac1796](https://doi.org/10.1093/mnras/stac1796)
- Clark, B. G. 1980, *A&A*, 89, 377
- Costa, E., Frontera, F., Heise, J., et al. 1997, *Nature*, 387, 783, doi: [10.1038/42885](https://doi.org/10.1038/42885)
- De Colle, F., Ramirez-Ruiz, E., Granot, J., & Lopez-Camara, D. 2012, *ApJ*, 751, 57, doi: [10.1088/0004-637X/751/1/57](https://doi.org/10.1088/0004-637X/751/1/57)
- De Pasquale, M., Page, M. J., Kann, D. A., et al. 2016, *MNRAS*, 462, 1111, doi: [10.1093/mnras/stw1704](https://doi.org/10.1093/mnras/stw1704)
- Djorgovski, S. G., Frail, D. A., Kulkarni, S. R., et al. 2001, *ApJ*, 562, 654, doi: [10.1086/323845](https://doi.org/10.1086/323845)
- Duncan, R. A., van der Horst, A. J., & Beniamini, P. 2023, *MNRAS*, 518, 1522, doi: [10.1093/mnras/stac3172](https://doi.org/10.1093/mnras/stac3172)
- Evans, P. A., Beardmore, A. P., Page, K. L., et al. 2009, *MNRAS*, 397, 1177, doi: [10.1111/j.1365-2966.2009.14913.x](https://doi.org/10.1111/j.1365-2966.2009.14913.x)
- Evans, P. A., Willingale, R., Osborne, J. P., et al. 2010, *A&A*, 519, A102, doi: [10.1051/0004-6361/201014819](https://doi.org/10.1051/0004-6361/201014819)
- Fausey, H. M., van der Horst, A. J., Tanvir, N. R., et al. 2025, *ApJ*, 985, 28, doi: [10.3847/1538-4357/adc5fc](https://doi.org/10.3847/1538-4357/adc5fc)
- Fong, W., Berger, E., Margutti, R., & Zauderer, B. A. 2015, *ApJ*, 815, 102, doi: [10.1088/0004-637X/815/2/102](https://doi.org/10.1088/0004-637X/815/2/102)
- Frail, D. A., Kulkarni, S. R., Nicastro, L., Feroci, M., & Taylor, G. B. 1997, *Nature*, 389, 261, doi: [10.1038/38451](https://doi.org/10.1038/38451)
- Frail, D. A., Soderberg, A. M., Kulkarni, S. R., et al. 2005, *ApJ*, 619, 994, doi: [10.1086/426680](https://doi.org/10.1086/426680)
- Frail, D. A., Waxman, E., & Kulkarni, S. R. 2000, *ApJ*, 537, 191, doi: [10.1086/309024](https://doi.org/10.1086/309024)
- Frail, D. A., Yost, S. A., Berger, E., et al. 2003, *ApJ*, 590, 992, doi: [10.1086/375193](https://doi.org/10.1086/375193)
- Freudling, W., Romaniello, M., Bramich, D. M., et al. 2013, *A&A*, 559, A96, doi: [10.1051/0004-6361/201322494](https://doi.org/10.1051/0004-6361/201322494)
- Gao, H., Lei, W.-H., Zou, Y.-C., Wu, X.-F., & Zhang, B. 2013, *NewAR*, 57, 141, doi: [10.1016/j.newar.2013.10.001](https://doi.org/10.1016/j.newar.2013.10.001)
- Gendre, B., Galli, A., Corsi, A., et al. 2007, *A&A*, 462, 565, doi: [10.1051/0004-6361:20065220](https://doi.org/10.1051/0004-6361:20065220)
- Giarratana, S., Giroletti, M., Spingola, C., et al. 2023, *A&A*, 670, A35, doi: [10.1051/0004-6361/202243829](https://doi.org/10.1051/0004-6361/202243829)
- Granot, J., De Colle, F., & Ramirez-Ruiz, E. 2018, *MNRAS*, 481, 2711, doi: [10.1093/mnras/sty2454](https://doi.org/10.1093/mnras/sty2454)
- Granot, J., & Sari, R. 2002, *ApJ*, 568, 820, doi: [10.1086/338966](https://doi.org/10.1086/338966)
- Harris, C. R., Millman, K. J., van der Walt, S. J., et al. 2020, *Nature*, 585, 357, doi: [10.1038/s41586-020-2649-2](https://doi.org/10.1038/s41586-020-2649-2)
- Högbom, J. A. 1974, *A&AS*, 15, 417
- Hunter, J. D. 2007, *Computing In Science & Engineering*, 9, 90, doi: [10.1109/MCSE.2007.55](https://doi.org/10.1109/MCSE.2007.55)
- Jakobsson, P., Hjorth, J., Fynbo, J. P. U., et al. 2004, *ApJL*, 617, L21, doi: [10.1086/427089](https://doi.org/10.1086/427089)
- Kilpatrick, C. D., Bom, C. R., Santos, A., Panda, S., & Navarete, F. 2023, *GRB Coordinates Network*, 34452, 1
- Klingler, N. J., Gronwall, C., Page, K. L., et al. 2023, *GRB Coordinates Network*, 34434, 1
- Laha, S., Barthelmy, S. D., Krimm, H. A., et al. 2023, *GRB Coordinates Network*, 34449, 1

- Lamb, G. P., Kann, D. A., Fernández, J. J., et al. 2021, *MNRAS*, 506, 4163, doi: [10.1093/mnras/stab2071](https://doi.org/10.1093/mnras/stab2071)
- Laskar, T., Alexander, K. D., Margutti, R., et al. 2023, *ApJL*, 946, L23, doi: [10.3847/2041-8213/acbfad](https://doi.org/10.3847/2041-8213/acbfad)
- Leung, J. K., Anderson, G. E., Ryder, S. D., et al. 2023, *GRB Coordinates Network*, 34518, 1
- Leung, J. K., Murphy, T., Ghirlanda, G., et al. 2021, *MNRAS*, 503, 1847, doi: [10.1093/mnras/stab326](https://doi.org/10.1093/mnras/stab326)
- Leung, J. K., Sharan Salafia, O., Spingola, C., et al. 2025, *arXiv e-prints*, arXiv:2502.13435, doi: [10.48550/arXiv.2502.13435](https://doi.org/10.48550/arXiv.2502.13435)
- Livio, M., & Waxman, E. 2000, *ApJ*, 538, 187, doi: [10.1086/309120](https://doi.org/10.1086/309120)
- MAGIC Collaboration, Acciari, V. A., Ansoldi, S., et al. 2019, *Nature*, 575, 455, doi: [10.1038/s41586-019-1750-x](https://doi.org/10.1038/s41586-019-1750-x)
- Mailyan, B., von Kienlin, A., Meegan, C., & Fermi Gamma-ray Burst Monitor Team. 2023, *GRB Coordinates Network*, 34440, 1
- Maity, B., & Chandra, P. 2021, *ApJ*, 907, 60, doi: [10.3847/1538-4357/abd2be](https://doi.org/10.3847/1538-4357/abd2be)
- Makhathini, S., Mooley, K. P., Brightman, M., et al. 2021, *ApJ*, 922, 154, doi: [10.3847/1538-4357/ac1ffc](https://doi.org/10.3847/1538-4357/ac1ffc)
- Matzner, C. D. 2003, *MNRAS*, 345, 575, doi: [10.1046/j.1365-8711.2003.06969.x](https://doi.org/10.1046/j.1365-8711.2003.06969.x)
- McKinney, W. 2010, in *Proceedings of the 9th Python in Science Conference*, ed. Stéfan van der Walt & Jarrod Millman, 56–61, doi: [10.25080/Majora-92bf1922-00a](https://doi.org/10.25080/Majora-92bf1922-00a)
- Mészáros, P., & Rees, M. J. 1997, *ApJ*, 476, 232, doi: [10.1086/303625](https://doi.org/10.1086/303625)
- Paczynski, B. 1986, *ApJL*, 308, L43, doi: [10.1086/184740](https://doi.org/10.1086/184740)
- Panaiteescu, A., & Kumar, P. 2000, *ApJ*, 543, 66, doi: [10.1086/317090](https://doi.org/10.1086/317090)
- Pe’er, A., & Wijers, R. A. M. J. 2006, *ApJ*, 643, 1036, doi: [10.1086/500969](https://doi.org/10.1086/500969)
- Piran, T. 2004, *Reviews of Modern Physics*, 76, 1143, doi: [10.1103/RevModPhys.76.1143](https://doi.org/10.1103/RevModPhys.76.1143)
- Racusin, J. L., Karpov, S. V., Sokolowski, M., et al. 2008, *Nature*, 455, 183, doi: [10.1038/nature07270](https://doi.org/10.1038/nature07270)
- Ramirez-Ruiz, E., García-Segura, G., Salmonson, J. D., & Pérez-Rendón, B. 2005, *ApJ*, 631, 435, doi: [10.1086/432433](https://doi.org/10.1086/432433)
- Rees, M. J., & Meszaros, P. 1992, *MNRAS*, 258, 41, doi: [10.1093/mnras/258.1.41P](https://doi.org/10.1093/mnras/258.1.41P)
- Resmi, L., Ishwara-Chandra, C. H., Castro-Tirado, A. J., et al. 2005, *A&A*, 440, 477, doi: [10.1051/0004-6361:20041642](https://doi.org/10.1051/0004-6361:20041642)
- Reynolds, J. 1994. <https://www.atnf.csiro.au/observers/memos/d96783~1.pdf>
- Rhodes, L., van der Horst, A. J., Fender, R., et al. 2020, *MNRAS*, 496, 3326, doi: [10.1093/mnras/staa1715](https://doi.org/10.1093/mnras/staa1715)
- Rhodes, L., van der Horst, A. J., Bright, J. S., et al. 2024, *MNRAS*, 533, 4435, doi: [10.1093/mnras/stae2050](https://doi.org/10.1093/mnras/stae2050)
- Roming, P. W. A., Koch, T. S., Oates, S. R., et al. 2009, *ApJ*, 690, 163, doi: [10.1088/0004-637X/690/1/163](https://doi.org/10.1088/0004-637X/690/1/163)
- Ryan, G., van Eerten, H., MacFadyen, A., & Zhang, B.-B. 2015, *ApJ*, 799, 3, doi: [10.1088/0004-637X/799/1/3](https://doi.org/10.1088/0004-637X/799/1/3)
- Salafia, O. S., & Ghirlanda, G. 2022, *Galaxies*, 10, 93, doi: [10.3390/galaxies10050093](https://doi.org/10.3390/galaxies10050093)
- Salafia, O. S., Ravasio, M. E., Yang, J., et al. 2022, *ApJL*, 931, L19, doi: [10.3847/2041-8213/ac6c28](https://doi.org/10.3847/2041-8213/ac6c28)
- Salvaterra, R. 2015, *Journal of High Energy Astrophysics*, 7, 35, doi: [10.1016/j.jheap.2015.03.001](https://doi.org/10.1016/j.jheap.2015.03.001)
- Sari, R., Piran, T., & Halpern, J. P. 1999, *ApJL*, 519, L17, doi: [10.1086/312109](https://doi.org/10.1086/312109)
- Sari, R., Piran, T., & Narayan, R. 1998, *ApJL*, 497, L17, doi: [10.1086/311269](https://doi.org/10.1086/311269)
- Sault, R. J., Teuben, P. J., & Wright, M. C. H. 1995, in *Astronomical Society of the Pacific Conference Series*, Vol. 77, *Astronomical Data Analysis Software and Systems IV*, ed. R. A. Shaw, H. E. Payne, & J. J. E. Hayes, 433
- Sault, R. J., & Wieringa, M. H. 1994, *A&AS*, 108, 585
- Schlegel, D. J., Finkbeiner, D. P., & Davis, M. 1998, *ApJ*, 500, 525, doi: [10.1086/305772](https://doi.org/10.1086/305772)
- Schneider, B., Chrimes, A., Malesani, D. B., et al. 2023, *GRB Coordinates Network*, 34467, 1
- Schulze, S., Klose, S., Björnsson, G., et al. 2011, *A&A*, 526, A23, doi: [10.1051/0004-6361/201015581](https://doi.org/10.1051/0004-6361/201015581)
- Shivvers, I., & Berger, E. 2011, *ApJ*, 734, 58, doi: [10.1088/0004-637X/734/1/58](https://doi.org/10.1088/0004-637X/734/1/58)
- Sironi, L., & Giannios, D. 2013, *ApJ*, 778, 107, doi: [10.1088/0004-637X/778/2/107](https://doi.org/10.1088/0004-637X/778/2/107)
- Skrutskie, M. F., Cutri, R. M., Stiening, R., et al. 2006, *AJ*, 131, 1163, doi: [10.1086/498708](https://doi.org/10.1086/498708)
- Speagle, J. S. 2020, *MNRAS*, 493, 3132, doi: [10.1093/mnras/staa278](https://doi.org/10.1093/mnras/staa278)
- Starling, R. L. C., Wijers, R. A. M. J., Hughes, M. A., et al. 2005, *MNRAS*, 360, 305, doi: [10.1111/j.1365-2966.2005.09042.x](https://doi.org/10.1111/j.1365-2966.2005.09042.x)
- Tingay, S. J., Jauncey, D. L., King, E. A., et al. 2003, *PASJ*, 55, 351, doi: [10.1093/pasj/55.2.351](https://doi.org/10.1093/pasj/55.2.351)
- van der Horst, A. J., Kouveliotou, C., Gehrels, N., et al. 2009, *ApJ*, 699, 1087, doi: [10.1088/0004-637X/699/2/1087](https://doi.org/10.1088/0004-637X/699/2/1087)
- van der Horst, A. J., Rol, E., Wijers, R. A. M. J., et al. 2005, *ApJ*, 634, 1166, doi: [10.1086/497021](https://doi.org/10.1086/497021)
- van der Horst, A. J., Kamble, A., Resmi, L., et al. 2008, *A&A*, 480, 35, doi: [10.1051/0004-6361:20078051](https://doi.org/10.1051/0004-6361:20078051)

- van der Horst, A. J., Paragi, Z., de Bruyn, A. G., et al. 2014, *MNRAS*, 444, 3151, doi: [10.1093/mnras/stu1664](https://doi.org/10.1093/mnras/stu1664)
- van Eerten, H., & MacFadyen, A. 2013, *ApJ*, 767, 141, doi: [10.1088/0004-637X/767/2/141](https://doi.org/10.1088/0004-637X/767/2/141)
- van Eerten, H. J., & MacFadyen, A. I. 2012, *ApJ*, 751, 155, doi: [10.1088/0004-637X/751/2/155](https://doi.org/10.1088/0004-637X/751/2/155)
- van Eerten, H. J., Meliani, Z., Wijers, R. A. M. J., & Keppens, R. 2011, *MNRAS*, 410, 2016, doi: [10.1111/j.1365-2966.2010.17582.x](https://doi.org/10.1111/j.1365-2966.2010.17582.x)
- van Paradijs, J., Groot, P. J., Galama, T., et al. 1997, *Nature*, 386, 686, doi: [10.1038/386686a0](https://doi.org/10.1038/386686a0)
- Virtanen, P., Gommers, R., Oliphant, T. E., et al. 2020, *Nature Methods*, 17, 261, doi: [10.1038/s41592-019-0686-2](https://doi.org/10.1038/s41592-019-0686-2)
- Wang, X.-G., Zhang, B., Liang, E.-W., et al. 2018, *ApJ*, 859, 160, doi: [10.3847/1538-4357/aabc13](https://doi.org/10.3847/1538-4357/aabc13)
- . 2015, *ApJS*, 219, 9, doi: [10.1088/0067-0049/219/1/9](https://doi.org/10.1088/0067-0049/219/1/9)
- Woosley, S. E. 1993, *ApJ*, 405, 273, doi: [10.1086/172359](https://doi.org/10.1086/172359)
- Zhang, W., & MacFadyen, A. 2009, *ApJ*, 698, 1261, doi: [10.1088/0004-637X/698/2/1261](https://doi.org/10.1088/0004-637X/698/2/1261)

## APPENDIX

## A. APPENDIX: POSTERIOR PARAMETER DISTRIBUTIONS

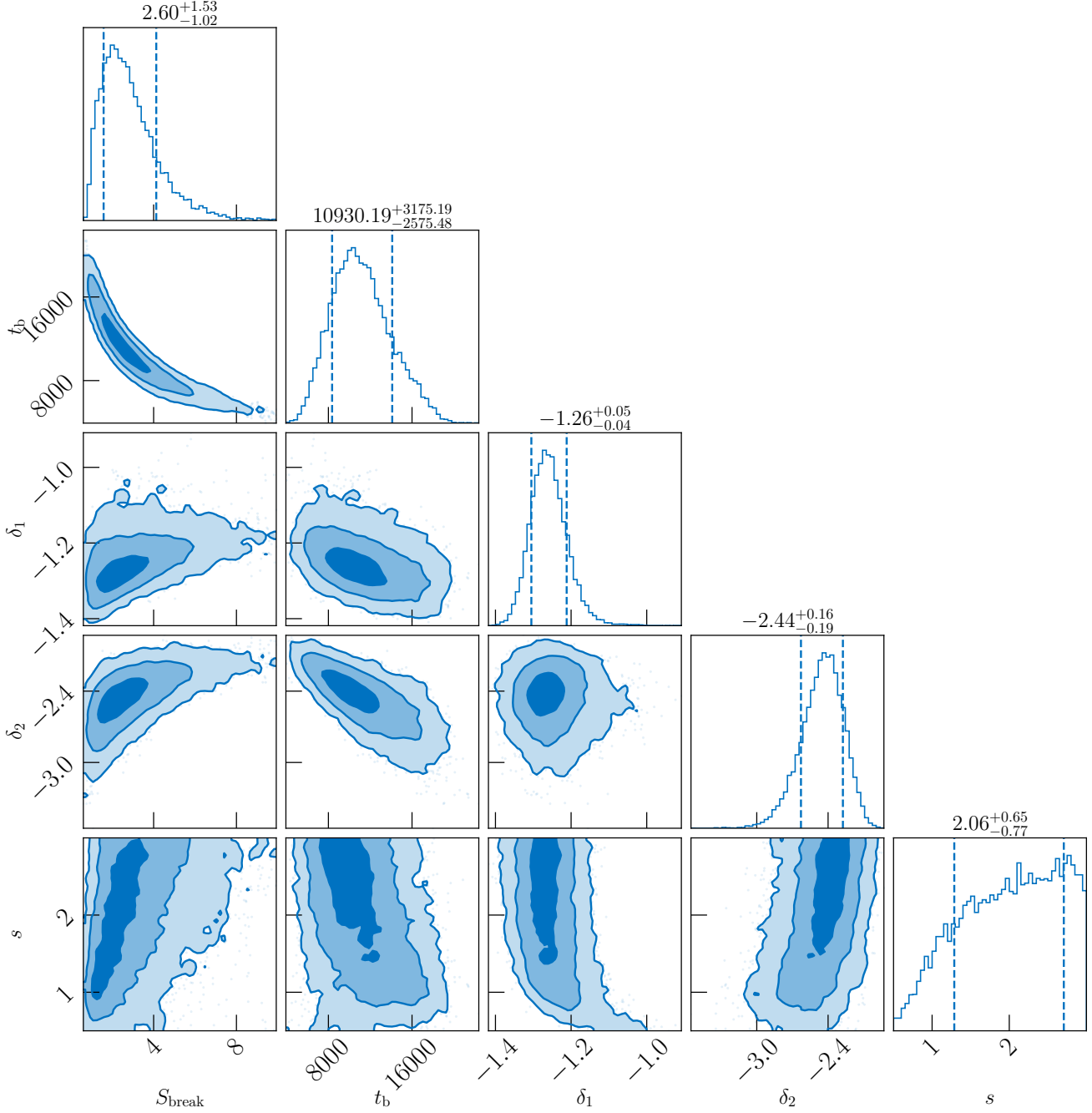


**Figure 8.** Posterior distributions of the parameters in the smoothly broken power-law model fit to the *Swift*/XRT light curve (see Table 3). The dashed vertical lines on the histograms represent the 68% credible interval of the corresponding marginalised posterior distribution.



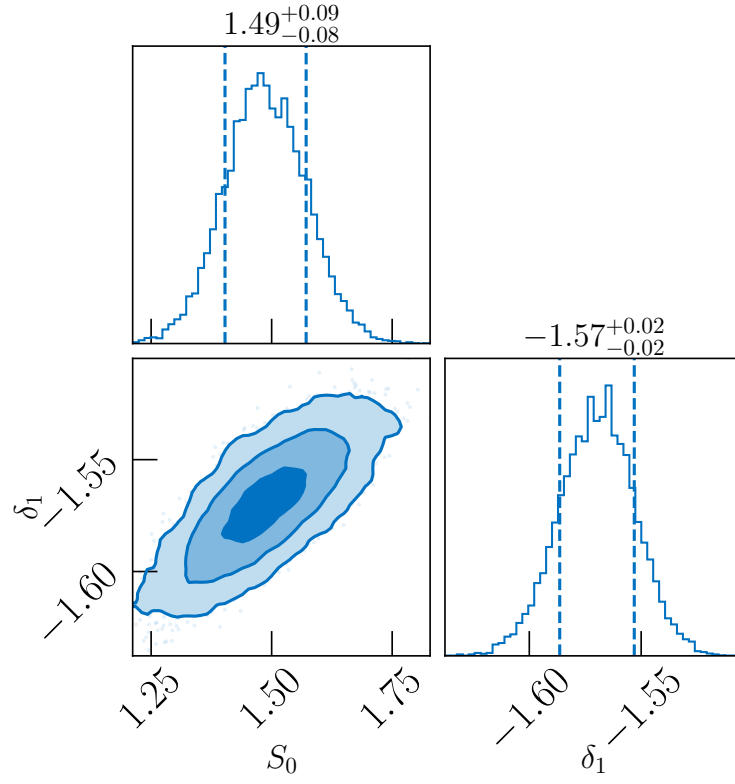


**Figure 9.** Similar to Figure 8 but for the power-law model fit of the *Swift*/XRT light curve (see Table 3).

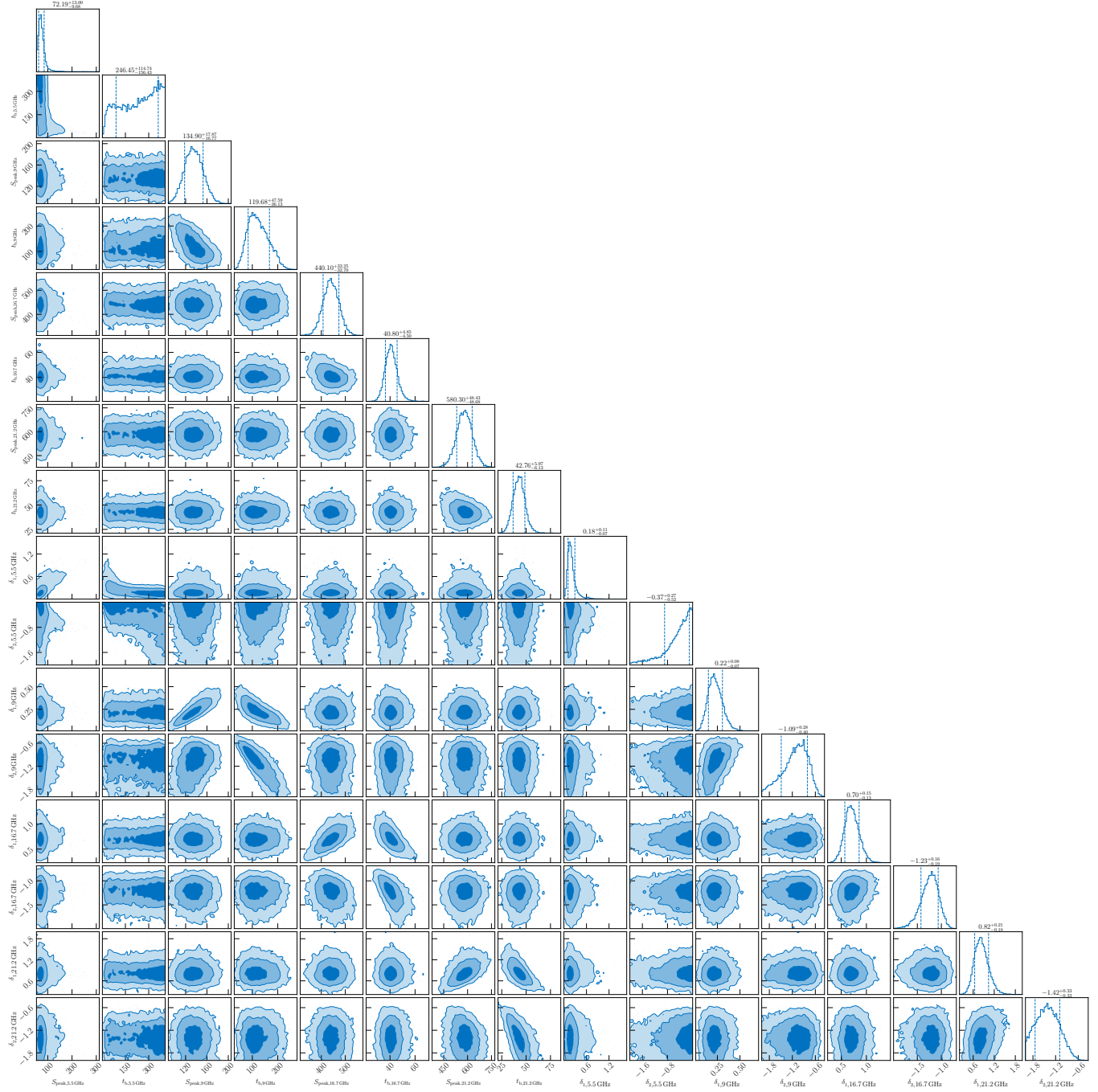


**Figure 10.** Posterior distributions of the parameters in the smoothly broken power-law model fit to the multi-frequency radio light curves assuming the rise and decay slopes ( $\delta_1$  and  $\delta_2$ ) are independent for each frequency (see Table 4). The dashed vertical lines on the histograms represent the 68% credible interval of the corresponding marginalised posterior distribution. To help with readability, the parameters from left to right are:  $S_{\text{peak},5.5 \text{ GHz}}$ ,  $t_{\text{b},5.5 \text{ GHz}}$ ,  $S_{\text{peak},9 \text{ GHz}}$ ,  $t_{\text{b},9 \text{ GHz}}$ ,  $S_{\text{peak},16.7 \text{ GHz}}$ ,  $t_{\text{b},16.7 \text{ GHz}}$ ,  $S_{\text{peak},21.2 \text{ GHz}}$ ,  $t_{\text{b},21.2 \text{ GHz}}$ ,  $\delta_{1,5.5 \text{ GHz}}$ ,  $\delta_{2,5.5 \text{ GHz}}$ ,  $\delta_{1,9 \text{ GHz}}$ ,  $\delta_{2,9 \text{ GHz}}$ ,  $\delta_{1,16.7 \text{ GHz}}$ ,  $\delta_{2,16.7 \text{ GHz}}$ ,  $\delta_{1,21.2 \text{ GHz}}$ , and  $\delta_{2,21.2 \text{ GHz}}$ .

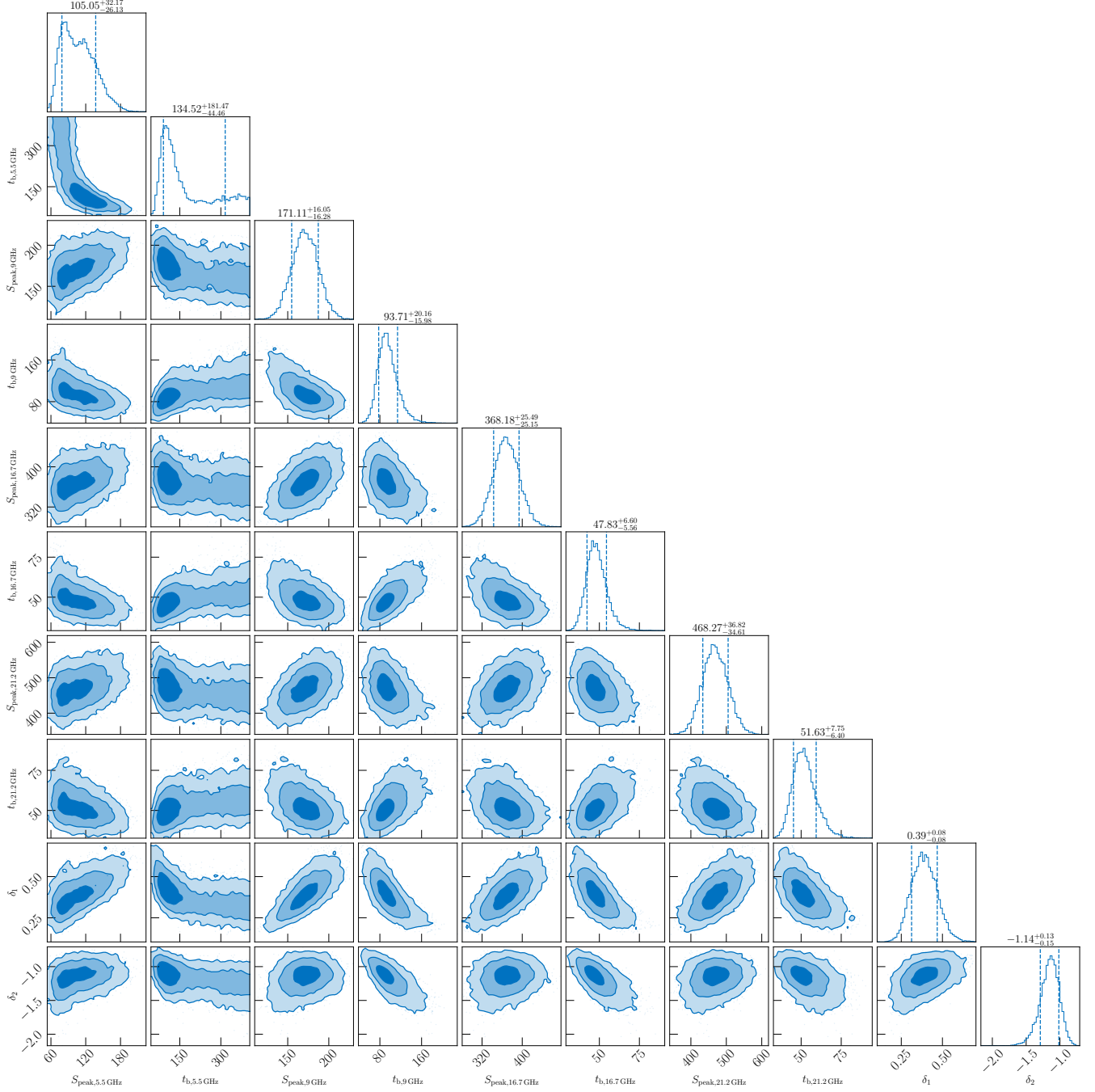


**Figure 11.** Similar to Figure 10 but for the smoothly broken power-law model fit to the multi-frequency radio light curves assuming the same rise and decay slopes ( $\delta_1$  and  $\delta_2$ ) at all frequencies (see Table 4).

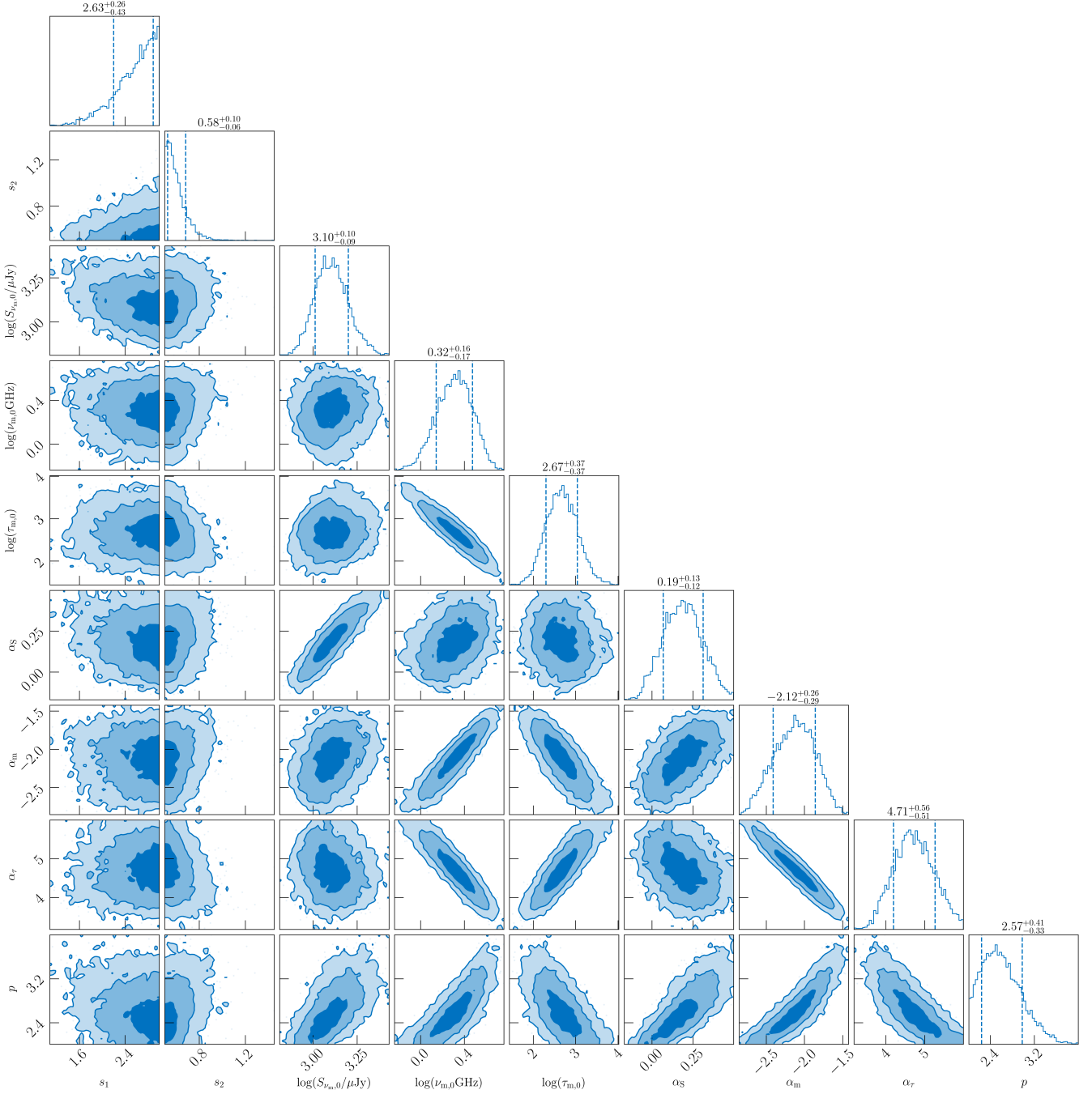


**Figure 12.** Posterior distributions of the parameters of the evolving synchrotron spectrum model of Subsection 3.4 (see Table 5). The dashed vertical lines on the histograms represent the 68% credible interval of the corresponding marginalised posterior distribution.